

# Distinct Berry Phases in a Single Triangular Möbius Microwave Resonator

E. C. I. Paterson,<sup>1,\*</sup> M. E. Tobar,<sup>1</sup> M. Goryachev,<sup>1</sup> and J. Bourhill<sup>1</sup>

<sup>1</sup>*Quantum Technologies and Dark Matter Labs, Department of Physics,  
University of Western Australia, 35 Stirling Hwy, 6009 Crawley, Western Australia.*

(Dated: January 13, 2026)

We report the experimental observation of two distinct Berry phases ( $+\frac{2\pi}{3}$  and  $-\frac{2\pi}{3}$ ) generated on the surface of a Möbius cavity resonator at microwave frequencies supporting the  $\text{TE}_{1,0,n}$  mode family. This resonator consists of a twisted, mirror-asymmetric prism with a cross-section of the triangular  $D_3$  symmetry group, bent around on itself to form a ring. This geometric class supports resonant modes with nonzero electromagnetic helicity (i.e. nonzero  $\vec{E} \cdot \vec{B}$  product) at microwave frequencies. There exist modes with three-fold rotational symmetry as well as those that exhibit no rotational symmetry. The latter result in an accumulated Berry phase whilst the former do not, which is determined from the measured frequency shift of the modes when compared to a mirror-symmetric resonator of otherwise equivalent geometry.

The Berry phase,  $\Pi$ , is a phase factor that arises in both quantum and classical systems undergoing cyclical evolution [1]. First observed in classical optics and molecular physics in the 1950s [2], it was later generalized by Sir Michael Berry in 1984. This phase has since been identified in diverse physical systems, including topological [3], acoustic [4], optical [3, 5, 6], chiroptical [7, 8], cosmological [9], condensed matter [10–12], and high-energy systems [13].

A particular form of Berry phase, called the spin-redirected phase, arises when a polarised light wave traverses a non-planar trajectory. In this case, the angular momentum of the wave undergoes a rotation in 3D space (corresponding to the special orthogonal group  $\text{SO}(3)$ ) as it is transported adiabatically along a closed path in momentum space, leading to the accumulation of a geometric phase shift [14, 15]. This phenomenon exemplifies holonomy: the wavevector accumulates a geometric phase over a closed loop as a result of its motion on a curved surface, such as that of a Möbius resonator [16]. In 2023, Wang et al. [3] experimentally observed a single Berry phase taking a value between 0 and  $0.7\pi$  in an optical dielectric Möbius strip, dependent on the rectangular cross-sectional aspect ratio, confirming predictions from earlier theoretical studies [17, 18].

Here, we investigate a microwave-frequency Möbius resonator with an equilateral triangle or  $D_3$  cross-section [19], which supports helical modes arising from its geometric asymmetry. Extending previous studies in the optical regime [3] to microwave frequencies, the present work demonstrates the generation of spin-redirected Berry phases in this Möbius resonator. Two

distinct Berry phases,  $+\frac{2\pi}{3}$  and  $-\frac{2\pi}{3}$ , are observed across different modes of a single cavity resonator. This behavior contrasts with the single Berry phase reported in rectangular cross-section Möbius resonators (see S9).

In particular contexts, such as under gauge invariant adiabatic evolution [20], the Berry phase is a key building block towards topological protection, which would render photonic modes resilient to dynamic perturbations, such as environmental noise [14]. The use of topological invariance in quantum encryption protocols, particularly for information encoding via prime factorization, has been demonstrated in the optical regime, leveraging coordinate transformations of 3D topologies, known as ‘framed knots’ [21] and as a potential application for the optical Möbius cavity [3].

The microwave Möbius resonators take the form of twisted  $D_3$  hollow prisms bent into closed rings, as shown in Fig. 1(a). The permissible twist angles are restricted to  $\phi = 2\pi r/3$  ( $r \in \mathbb{Z}$ ), ensuring that the joining faces match.

The spin-redirected Berry phase arises from the reorientation of the electromagnetic wave’s angular momentum during its non-trivial evolution in parameter space, with the geometric twist acting as a rotation in momen-

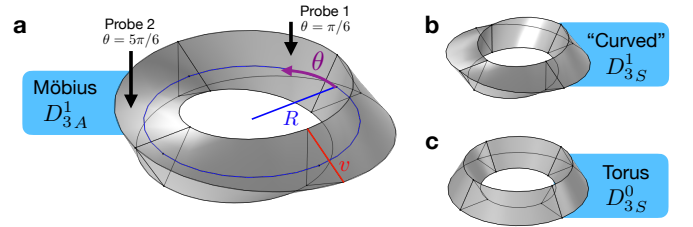


Figure 1. Examples of the geometries considered; (a) the  $D_{3A}^1$  resonator, (b) the  $D_{3S}^1$  resonator and (c) the  $D_{3S}^0$  resonator.

\* 22734222@student.uwa.edu.au

tum space ( $k$ -space) [14].

In each circulation, the wavevector rotates by  $2\pi r/3$ , corresponding to the solid angle swept in momentum space [15, 22–24]. Over three consecutive revolutions, the tip of the wavevector traces out a closed loop of latitude on the Poincaré sphere, reflecting the cyclic trajectories followed by photons in the twisted ring geometry.

This geometry is a class of electromagnetic resonator that permits the existence of resonant modes with near-unity normalised electromagnetic helicity [19, 25],  $\mathcal{H}_n$ , which is a quantity proportional to a resonant mode's  $\vec{E} \cdot \vec{B}$  scalar product.  $\mathcal{H}_n$  measures the degree of mixing between the electric and magnetic fields [26–29] (see S7). However, as explained later in this work, a Berry phase is only observed for the lower-order quasi transverse electric (TE) modes, which exhibit lower  $\mathcal{H}_n$ .

Reversing the cavity twist halfway along its length (eliminating net twist) results in the wavevector returning to its initial orientation after one circulation, yielding no net geometric phase accumulation. This configuration, referred to as the mirror-symmetric curved cavity and shown in Fig. 1(b), is topologically equivalent (homeomorphic) to the torus resonator depicted in Fig. 1(c), which is a ring resonator with no twist ( $\phi = 0$ ) [3]. As the torus resonator is not curved and maintains mirror symmetry, it likewise does not accumulate a geometric phase.

To characterise these geometries, the notation  $D_{sx}^r$  is adopted, where  $D_s$  specifies the  $s$ -fold dihedral symmetry of the resonator cross-section,  $r$  indicates the absolute number of full rotations of the cross-section along the closed path, and  $x$  identifies the global symmetry of the resonator,  $A$  denoting asymmetric Möbius-type geometries, and  $S$  corresponding to mirror-symmetric structures. The  $TE_{m,p,n}$  modes in the twisted resonators are characterised by three integers. The mode numbers  $m$  and  $p$  represent the number of variations in the standing wave pattern within the transverse plane of the cavity cross-section, while  $n$  corresponds to the number of variations along the azimuthal direction.

The interference of out-of-phase counter-propagating waves travelling within the  $D_3^{r \neq 0} A$  resonator gives rise to standing wave patterns characterised by a fractional number of variations along the resonator's azimuthal direction [3]. The observation of  $n = \mathbb{Z} \pm \frac{1}{3}$  azimuthal mode numbers in the  $D_3^{r \neq 0} A$  resonator directly confirms the presence of Berry phases. As the polarisation remains unchanged along the photon path, these phases can be classified as spin-redirection Berry phases. In contrast, in a  $D_3^r S$  resonator, the counter-propagating waves interfere in phase, resulting in resonant modes with integer  $n$ . In this

work, we focus on the lowest-order  $TE_{1,0,n}$  mode family rather than the higher-order modes with near-unity  $\mathcal{H}_n$ , as the latter exhibit rotational symmetry [19, 25], ensuring they always return in phase after completing a closed loop around the  $D_3^{r \neq 0} A$  resonator (see S8 A). In contrast, the  $TE_{1,0,n}$  modes lack rotational symmetry so after completing a full circuit of the resonator, the  $TE_{1,0,n}$  modes exhibit a  $2\pi r/3$  phase offset with themselves, leading to the characteristic out-of-phase interference.

The  $D_{3A}^1$ ,  $D_{3A}^2$ ,  $D_{3A}^3$  and  $D_{3S}^0$  resonators were simulated using finite element modelling (FEM) for a cavity with a radius  $R = 79.58$  mm and cross-sectional vertex length  $v = 20$  mm. The azimuthal mode number  $n$  for the  $TE_{1,0,n}$  mode family was determined from the eigen-solutions by counting the anti-nodes of the tangential surface current density  $|\mathbf{K}_\tau|$  over a complete loop of the resonator. Surface current densities exhibit two tangents: the azimuthal ( $\mathbf{K}_{\beta\perp}$ ) and the in-plane tangential component, with the former arbitrarily chosen for this analysis. To calculate  $n$ , which originates from a  $e^{in\theta}$  term in the eigenvector expression, the number of anti-nodes was divided by the number of "windings" and then divided by two to account for  $2n$  anti-nodes in  $2\pi$  radians. For the  $D_{3A}^1$  and  $D_{3A}^2$  resonators, three windings are required to complete a closed loop, while only one winding suffices for the  $D_{3S}^0$  and the  $D_{3A}^3$  resonators. This method of determining the bulk resonator mode number via surface current density leverages the holographic principle, which posits that the information within a 3D volume can be encoded on a 2D surface [30, 31]. Figures 2(a) and 2(b) illustrate this concept for two configurations of the  $TE_{1,0,n}$  mode family. The electric field of these modes in the resonator bulk originates from the negatively charged surface and terminates on the positively charged surface.

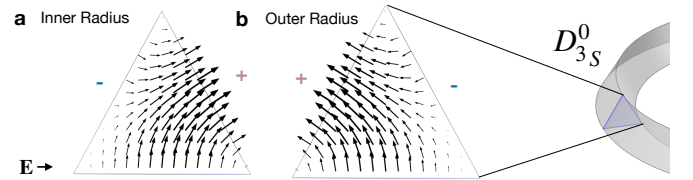


Figure 2. The cross-section of the FEM simulated  $D_{3S}^0$  resonator showing the charge on the surface and electric field pattern in the bulk of the resonator for the  $TE_{1,0,n}$  modes that have preferentially built up charge on the (a) inner surface of the resonator and (b) the outer surface of the resonator, resulting in a non-degenerate doublet pair. This doublet splitting defines the spectral gap within which the fractional modes of the twisted  $D_{3A}^1$  and  $D_{3A}^2$  resonators shift into as a result of the accumulated  $\Pi_{(n,j)}$ .

Each  $\text{TE}_{1,0,n}$  mode in the  $D_{3S}^r$  resonators exists as a pair of doublet solutions which are split in frequency due to differences in the radii of the dominant resonator surfaces: the inner surface, with a smaller radius, and the outer surface, with a larger radius. For a given mode number  $n$ , modes that induce a positive charge on the inner surface exhibit higher resonant frequencies than those associated with a positive charge on the outer surface. Each of these non-degenerate doublets is further split into a degenerate pair of orthogonal modes with  $\cos(n\theta)$  or  $\sin(n\theta)$  azimuthal field dependence, corresponding to the two standing-wave solutions formed by the interference of counter-propagating waves around the resonator, yielding a total of four modes for each  $n$ .

From the FEM simulations of the  $D_{3A}^1$  and  $D_{3A}^2$  resonators, the  $|\mathbf{K}_{\beta\perp}|$  surface plots confirmed the existence of  $\text{TE}_{1,0,n}$  modes with  $n = \mathbb{Z} \pm \frac{1}{3}$  and hence the presence of spin-redirection Berry phase. Fig. 3(a) illustrates this for the  $\text{TE}_{1,0,15\frac{2}{3}}$  mode in the  $D_{3A}^1$  resonator. In contrast, the  $D_{3S}^0$  resonator, which is topologically equivalent to any  $D_{3S}^r$  resonator, exhibits integer mode numbers, as shown for the  $\text{TE}_{1,0,16}$  mode in Fig. 3(b). This aligns with the expected absence of accumulated Berry phase. Note that the  $D_{3A}^1$  resonator also demonstrated only integer mode numbers, because after one full circulation of the cavity the wavevector will have rotated by  $2\pi$  (see S3).

The  $\text{TE}_{1,0,n}$  mode frequencies for both the  $D_{3A}^1$  and  $D_{3S}^0$  resonators follow the same modal spectrum, as depicted in Fig. 3(c). Notably, the frequencies of the  $n = \mathbb{Z} \pm \frac{1}{3}$  modes in the  $D_{3A}^1$  resonator occur between the two doublets of the  $n = \mathbb{Z}$  modes of the  $D_{3S}^0$  resonator. For the positive  $\mathcal{H}_n$  modes in the  $D_{3A}^1$  resonator, this frequency shift is positive, requiring a mode number adjustment of  $\Delta n = +\frac{1}{3}$ . Conversely, for the negative  $\mathcal{H}_n$  modes, the frequency shift is negative, corresponding to  $\Delta n = -\frac{1}{3}$ . These frequency shifts are directly linked to the Berry phase, which accounts for the adjustment needed to align the fractional  $n = \mathbb{Z} \pm \frac{1}{3}$  modes in the  $D_{3A}^1$  resonator with the integer modes of the  $D_{3S}^0$  resonator. This relationship for the  $D_3$  resonators considered in this paper is expressed as (see S1 G):

$$\Pi_{(n,j)} = \Delta f_{(n,j)} \frac{4\pi^2 R}{c \sqrt{1 - \left(\frac{2c}{3vf_{(n,j)}^S}\right)^2}}, \quad (1)$$

where  $\Delta f_{(n,j)} = f_{(n,j)+\Delta n}^A - f_{(n,j)}^S$  denotes the frequency difference between the  $\text{TE}_{1,0,(n,j)+\Delta n}$  mode in the  $D_{3A}^{r \neq 0}$  resonator ( $f_{(n,j)+\Delta n}^A$ ) and the  $\text{TE}_{1,0,(n,j)}$  mode in the  $D_{3S}^r$  resonator ( $f_{(n,j)}^S$ ), for integer  $n$ , and  $c$  is the speed of light

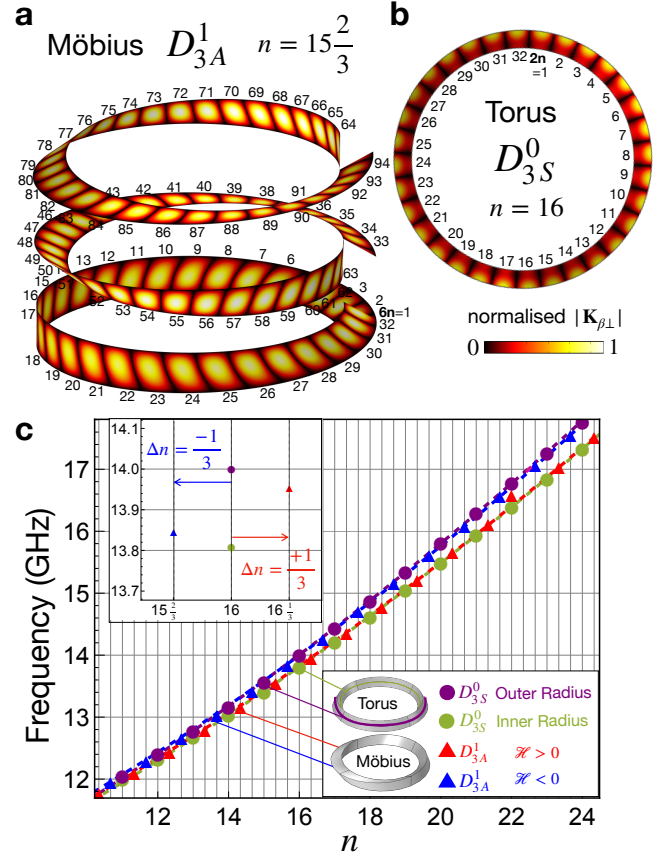


Figure 3. The surface plots of  $|\mathbf{K}_{\beta\perp}|$  for the (a)  $\text{TE}_{1,0,15\frac{2}{3}}$  mode in the  $D_{3A}^1$  resonator and the (b)  $\text{TE}_{1,0,16}$  mode in the  $D_{3S}^0$  resonator. The number of antinodes are shown: for the  $D_{3A}^1$  resonator, a closed loop requires three windings, each contributing  $2n$  antinodes, yielding a total of  $6n$ ; for the  $D_{3S}^0$ , one winding suffices, giving  $2n$  antinodes. (c) The modal spectrum of the  $\text{TE}_{1,0,n}$  modes as a function of  $n$  for the  $D_{3A}^1$  and  $D_{3S}^0$  resonators.

in vacuum. Here,  $j \in \{1, 2, 3, 4\}$  indexes the four internal eigenchannels (two  $\pm \mathcal{H}_n$  branches times the two standing-wave parities  $\cos(n\theta)$  and  $\sin(n\theta)$ ), each acquiring its own geometric phase  $\Pi_{(n,j)}$ .

In general, it is preferable to take  $f_{(n,j)}^S$  from the resonant modes in the  $D_{3S}^r$  resonator when calculating (1), rather than from the  $D_{3A}^r$  resonator. This choice ensures that the frequency shift observed between the  $D_{3A}^r$  and  $D_{3A}^{r \neq 0}$  resonators arises solely from geometric phase accumulation rather than from curvature effects. However, as shown in Fig. 4, the resonant frequencies of the  $D_{3S}^0$  and  $D_{3A}^{r \neq 0}$  resonators are equivalent for the case of the

$TE_{1,0,n}$  modes. Leveraging this equivalence, the  $\Delta f_{(n,j)}$  values used to calculate  $\Pi_{(n,j)}$  are taken relative to the  $D_{3S}^0$  resonator, simplifying FEM simulations and mode identification. Note that this equivalency is no longer true for the next family of modes up,  $TE_{1,1,n+1}$  and  $TM_{1,1,n}$ . These modes are degenerate in frequency for a  $D_{3S}^0$  resonator and as a twist is introduced they undergo magnetolectric coupling and tune in frequency due to a mechanism explained in [19, 25] resulting in the resonant frequencies no longer agreeing with the  $D_{3S}^{r \neq 0}$  and  $D_{3S}^0$  configurations (see S8 B).

Applying (1) to the simulated eigenfrequencies, it is observed that as  $n$  increases, the  $D_{3A}^1$  resonator asymptotically approaches two distinct Berry phases of equal magnitude  $\frac{2\pi}{3}$ , but with opposite signs. These distinct Berry phases correspond to the  $TE_{1,0,n}$  modes with opposing electromagnetic helicities  $\mathcal{H}_n$ , as demonstrated in Fig. 5. Specifically, the positive  $\Pi_{(n,j)}$  is associated with the  $TE_{1,0,n}$  mode possessing  $\mathcal{H} > 0$ , while the negative  $\Pi_{(n,j)}$  corresponds to the  $TE_{1,0,n}$  mode with  $\mathcal{H}_n < 0$ . The emergence of  $\mathcal{H}_n$  in the  $TE_{1,0,n}$  modes is attributed to their self-interference as they travel the closed-loop of the twisted resonator.

For the  $D_{3A}^2$  resonator, an opposite frequency shift behaviour is observed with respect to the  $\mathcal{H}_n$  signs of the  $TE_{1,0,n}$  modes. This results in Berry phases equal in magnitude to those of the  $D_{3A}^1$  resonator but with reversed signs for the respective  $\mathcal{H}_n$  (see S3).

To confirm the expected frequency shift between the  $D_{3A}^1$  resonator and the  $D_{3S}^1$  resonator, 3D-printed aluminium resonators were fabricated using selective laser melting (SLM) [32]. The dimensions of these resonators were measured to be  $v = 19.92 \pm 0.01$  mm and  $R = 23.67 \pm 0.04$  mm. This resonator is smaller in diameter than the simulated designs above due to dimensional constraints of the printing process, and thus its approximation as an infinitely long waveguide is less accurate

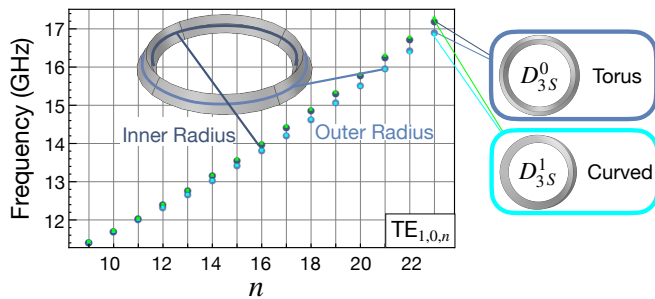


Figure 4. The eigenfrequencies of the  $D_{3S}^0$  and  $D_{3S}^1$  resonators as a function of axial mode number  $n$  for the  $TE_{1,0,n}$  modes.

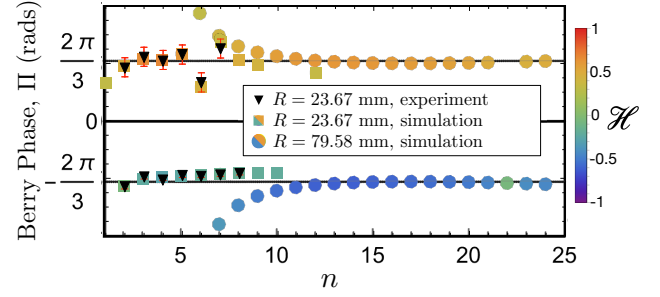


Figure 5.  $\Pi_{(n,j)}$  as a function of  $n$  for the  $TE_{1,0,n}$  modes in the  $D_{3A}^1$  resonator for  $R = 23.67$  mm (simulated and experimental) and  $R = 79.58$  mm (simulated), with associated  $\mathcal{H}_n$  depicted by colour. Asymptotic limits of  $\pm 2\pi/3$  are shown as black lines. Error bars on the experimental results represent systematic errors.

(see S6). As such, the group velocity formula based on the cutoff wavenumber used to derive (1) (see S1 F) is less accurate for this case. The resonator consisted of two sections: a “universal” half, common to all configurations, and a modular second half that was either mirror-symmetric or asymmetric. Excitation was achieved via two probes inserted into the universal half of the cavity and aligned along the  $z$ -axis. Both probes are coaxial antennae, the first, located at  $\theta = \frac{\pi}{6}$ , has a straight length of inner conductor exposed so as to couple to the  $E_z$  component of the cavity field. The second probe, located at  $\theta = \frac{5\pi}{6}$ , has the exposed inner conductor bent into a loop and soldered to the outer conductor, coupling to the  $H_\theta$  component. These placements are illustrated in Fig. 1(a). This modular cavity design minimised the number of unique components needed for fabrication and ensured consistent probe positioning across all measurements. The printed resonators are shown in Fig. 6.

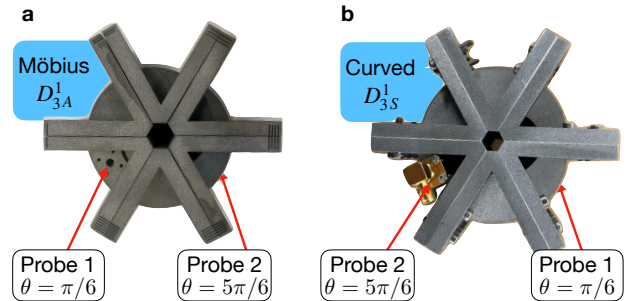


Figure 6. The (a)  $D_{3A}^1$  and (b)  $D_{3S}^1$  3D-printed aluminium resonators with dimensions  $v = 19.92 \pm 0.01$  mm and  $R = 23.67 \pm 0.04$  mm.

The transmission spectra measured through the resonators are compared to the eigenfrequencies obtained from FEM simulations of the  $D_{3A}^1$  and  $D_{3S}^1$  resonators, as shown by the gridlines in Fig. 7(a). A strong agreement is observed between the transmission peak frequencies and the simulation results, validating the experimental measurements. From the transmission peak frequencies in Fig. 7(b), the predicted inner–outer non-degeneracy of the  $TE_{1,0,5}$  modes in the  $D_{3S}^1$  resonator is observed. The  $TE_{1,0,4\frac{2}{3}}$  and  $TE_{1,0,5\frac{1}{3}}$  modes in the  $D_{3A}^1$  resonator have frequencies that lie between these  $TE_{1,0,5}$  modes (see S4 for experimental mode number methodology). These results confirm the observation of Berry phases, with the experimentally measured frequency shifts matching those predicted by simulation, and derived Berry phase results (see S5) presented in Fig. 5, which similar to the larger  $R$  case, take values of  $\pm\frac{2\pi}{3}$ . This demonstrates the topological nature of the Berry phase: despite the resonators having different values of  $R$ , and therefore different dynamical phases reflected in their resonant frequencies, the geometric contribution to the phase is identical due to their topological equivalence.

It should be noted that each transmission peak in Fig. 7(b) corresponds to a pair of degenerate modes whose azimuthal field distributions exhibit  $\cos(n\theta)$  and  $\sin(n\theta)$  angular dependence in the closed-ring resonator. This degeneracy, however, cannot be resolved in the measured transmission spectrum due to the limited Q-factor ( $Q \sim 5 \times 10^2$ ) of the experimental cavity. Because these modes form a degenerate doublet, their adiabatic transport around the closed path is governed by a non-Abelian Berry connection, and the accumulated geometric phase is encoded in the corresponding holonomy acting on this degenerate subspace (see S1). For comparison, the transmission spectrum of the linear cavity, obtained by unwrapping the  $D_3$  twisted prism from its closed-ring configuration, is also shown. In this geometry, no  $\Pi_{(n,j)}$  is accumulated because the propagation path is not cyclic. Consequently, the inner- and outer-surface modes that are non-degenerate in the ring become degenerate, and the azimuthal  $\sin(n\theta)$ -like mode is prohibited by the conducting boundary conditions at the endfaces, leaving a single axial dependence of the form  $\cos(q\pi z/L)$ , where  $q$  counts half-wavelengths between reflective boundaries ( $L = q\lambda_z/2$ ) rather than full wavelengths around a closed path ( $2\pi R = n\lambda_\phi$ ). The apparent doubling of the mode index therefore arises purely from the change in naming convention when transitioning from azimuthal to axial mode counting.

We observe good agreement between simulated and experimental Berry phase for modes in the  $R = 23.67$  mm  $D_{3A}^1$  resonator, with the deviation from the  $\pm 2\pi/3$

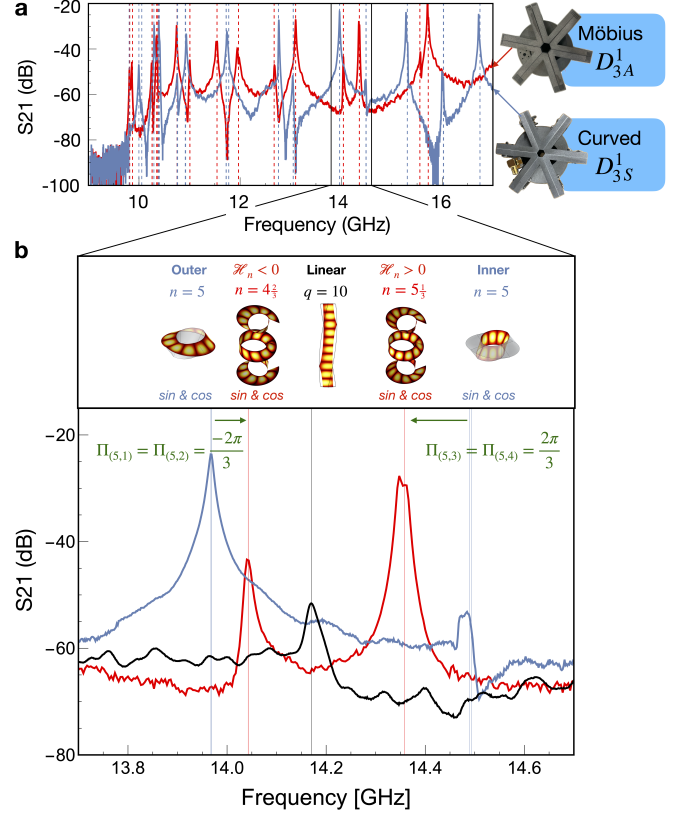


Figure 7. (a) Experimental  $S_{21}$  transmission measurements of the  $D_{3S}^1$  (blue) and the  $D_{3A}^1$  (red) resonators. The gridlines, colour-coded to match the respective measurements, mark the simulated resonant frequencies of the  $TE_{1,0,n}$  modes for each resonator. These 3D-printed cavities are shown on the right. (b) A magnified view of the transmission spectra highlighting the  $TE_{1,0,5}$  mode of the  $D_{3S}^1$  resonator and the  $TE_{1,0,4\frac{2}{3}}$  and  $TE_{1,0,5\frac{1}{3}}$  modes of the  $D_{3A}^1$  resonator. For comparison, the transmission of a linear cavity with identical dimensions is also shown for the  $TE_{1,0,10}$  mode.

asymptotes for modes around  $n \approx 6$  attributed to mode hybridisation with the next higher-order mode family, which emerges near 17 GHz as shown in Fig. S9. This hybridisation is evident from the drop in  $\mathcal{H}_n$  around  $n \approx 6$  in Fig. 5.

The generation of Berry phases relies critically on two conditions: 1. the angular momentum of the electromagnetic radiation must undergo a rotation relative to its initial configuration, achieved here via twisting, that induces a transformation in momentum space; and 2. the radiation must follow a closed path in momentum space, ensuring that the electromagnetic waves in the resonator interfere out of phase. These criteria are satisfied by the

looped geometry of the Möbius resonator. Due to the  $D_3$  cross-section of this Möbius resonator, it supports Berry phases of  $\Pi_{(n,j)} = s_j \frac{2\pi}{3}$  ( $s_j = -1, -1, +1, +1$ ) when twisted by a non-integer multiple of  $2\pi$ . Notably, this study represents the first observation of these two distinct Berry phases within two types of monochromatic, electromagnetic modes in a single empty cavity resonator, only governed by boundary conditions.

This work was funded by the Australian Research

Council Centre of Excellence for Engineered Quantum Systems, CE170100009 and Centre of Excellence for Dark Matter Particle Physics, CE200100008. E.C.P is partially funded through the Defence Science Centre Research Higher Degree Student Grant. This work used the NCRIS and Government of South Australia enabled Australian National Fabrication Facility - South Australian Node (ANFF-SA).

All data and FEM model parameters are available upon request to the authors.

- 
- [1] M. V. Berry. Quantal Phase Factors Accompanying Adiabatic Changes. *Proceedings of the Royal Society of London Series A*, 392(1802):45–57, March 1984.
- [2] S. Pancharatnam. Generalized theory of interference, and its applications. *Proceedings of the Indian Academy of Sciences - Section A*, 44(5):247–262, November 1956.
- [3] Jiawei Wang, Sreeramulu Valligatla, Yin Yin, Lukas Schwarz, Mariana Medina-Sánchez, Stefan Baunack, Ching Hua Lee, Ronny Thomale, Shilong Li, Vladimir M. Fomin, Libo Ma, and Oliver G. Schmidt. Experimental observation of Berry phases in optical Möbius-strip microcavities. *Nature Photonics*, 17(1):120–125, January 2023.
- [4] Meng Xiao, Guancong Ma, Zhiyu Yang, Ping Sheng, Z. Q. Zhang, and C. T. Chan. Geometric phase and band inversion in periodic acoustic systems. *Nature Physics*, 11(3):240–244, March 2015.
- [5] H. P. Breuer, K. Dietz, and M. Holthaus. Berry’s phase in quantum optics. *Phys. Rev. A*, 47:725–728, Jan 1993.
- [6] Y. Q. Cai, G. Papini, W. R. Wood, and S. R. Valluri. On the classical origin of Berry’s phase for photons. *Quantum Optics*, 1(1):49–52, September 1989.
- [7] Raouf Barboza, Umberto Bortolozzo, Marcel G. Clerc, and Stefania Residori. Berry Phase of Light under Bragg Reflection by Chiral Liquid-Crystal Media. *Phys. Rev. Lett.*, 117(5):053903, July 2016.
- [8] Lin Zhu, Chun-Ting Xu, Peng Chen, Yi-Heng Zhang, Si-Jia Liu, Quan-Ming Chen, Shi-Jun Ge, Wei Hu, and Yan-Qing Lu. Pancharatnam-Berry phase reversal via opposite-chirality-coexisted superstructures. *Light: Science & Applications*, 11(1):135, May 2022.
- [9] Dhurjati Prasad Datta. Geometric phase in vacuum instability: Applications in quantum cosmology. *Phys. Rev. D*, 48(12):5746–5750, December 1993.
- [10] Jing Wang and Shou-Cheng Zhang. Topological states of condensed matter. *Nature Materials*, 16(11):1062–1067, November 2017.
- [11] Yuanbo Zhang, Yan-Wen Tan, Horst L. Stormer, and Philip Kim. Experimental observation of the quantum Hall effect and Berry’s phase in graphene. *Nature (London)*, 438(7065):201–204, November 2005.
- [12] Raffaele Resta. REVIEW ARTICLE: Manifestations of Berry’s phase in molecules and condensed matter. *Journal of Physics Condensed Matter*, 12(9):R107–R143, March 2000.
- [13] Hidenori Sonoda. Berry’s phase in chiral gauge theories. *Nuclear Physics B*, 266(2):410–422, March 1986.
- [14] Ahmed H. Dorrah, Michele Tamagnone, Noah A. Rubin, Aun Zaidi, and Federico Capasso. Introducing Berry phase gradients along the optical path via propagation-dependent polarization transformations. *Nanophotonics*, 11(4):713–725, 2022.
- [15] Akira Tomita and Raymond Y. Chiao. Observation of Berry’s topological phase by use of an optical fiber. *Phys. Rev. Lett.*, 57:937–940, Aug 1986.
- [16] Josef W. Zwanziger, Markus Koenig, and Alexander Pines. Berry’s phase. *Annual Review of Physical Chemistry*, 41:601–646, 1990.
- [17] Jakob Kreissmann and Martina Hentschel. The optical Möbius strip cavity: Tailoring geometric phases and far fields. *EPL (Europhysics Letters)*, 121(2):24001, January 2018.
- [18] S. L. Li, L. B. Ma, V. M. Fomin, S. Böttner, M. R. Jorgensen, and O. G. Schmidt. Non-integer optical modes in a Möbius-ring resonator. *arXiv e-prints*, page arXiv:1311.7158, November 2013.
- [19] J. F. Bourhill, E. C. I. Paterson, M. Goryachev, and M. E. Tobar. Searching for ultralight axions with twisted cavity resonators of anyon rotational symmetry with bulk modes of nonzero helicity. *Phys. Rev. D*, 108(5):052014, September 2023.
- [20] Y. Aharonov and J. Anandan. Phase change during a cyclic quantum evolution. *Phys. Rev. Lett.*, 58:1593–1596, Apr 1987.
- [21] Hugo Larocque, Alessio D’Errico, Manuel F. Ferrer-Garcia, Avishy Carmi, Eliahu Cohen, and Ebrahim Karimi. Optical framed knots as information carriers. *Nature Communications*, 11:5119, October 2020.
- [22] Konstantin Y. Bliokh, Avi Niv, Vladimir Kleiner, and Erez Hasman. Geometrodynamics of spinning light. *Nature Photonics*, 2(12):748–753, December 2008.
- [23] Raymond Y. Chiao and Yong-Shi Wu. Manifestations of Berry’s topological phase for the photon. *Phys. Rev. Lett.*, 57:933–936, Aug 1986.
- [24] Miguel Alonso and Mark Dennis. The geometric phase

- made simple. *Photoniques*, pages 58–63, 11 2022.
- [25] E. C. I. Paterson, J. Bourhill, M. E. Tobar, and M. Goryachev. Electromagnetic helicity in twisted cavity resonators. *Phys. Rev. A*, 112:013530, Jul 2025.
- [26] F. Alpeggiani, K. Y. Bliokh, F. Nori, and L. Kuipers. Electromagnetic helicity in complex media. *Phys. Rev. Lett.*, 120:243605, Jun 2018.
- [27] Konstantin Y. Bliokh, Yuri S. Kivshar, and Franco Nori. Magnetoelectric effects in local light-matter interactions. *Phys. Rev. Lett.*, 113:033601, Jul 2014.
- [28] Josep Martínez-Romeu, Iago Diez, Sebastian Golat, Francisco J. Rodríguez-Fortu no, and Alejandro Martínez. Chiral forces in longitudinally invariant dielectric photonic waveguides. *Photon. Res.*, 12(3):431–443, Mar 2024.
- [29] Konstantin Y Bliokh, Aleksandr Y Bekshaev, and Franco Nori. Dual electromagnetism: helicity, spin, momentum and angular momentum. *New Journal of Physics*, 15(3):033026, mar 2013.
- [30] Chris Fields, James F. Glazebrook, and Antonino Marciano. The physical meaning of the holographic principle. *arXiv e-prints*, page arXiv:2210.16021, October 2022.
- [31] Raphael Bousso. *The Holographic Principle*, pages 75–166. Springer Netherlands, Dordrecht, 2003.
- [32] Daniel L. Creedon, Maxim Goryachev, Nikita Kostylev, Timothy B. Sercombe, and Michael E. Tobar. A 3d printed superconducting aluminium microwave cavity. *Applied Physics Letters*, 109(3):032601, 2016.
- [33] F. Wilczek and A. Zee. Appearance of gauge structure in simple dynamical systems. *Phys. Rev. Lett.*, 52:2111–2114, 1984.
- [34] A. Shapere and F. Wilczek, editors. *Geometric Phases in Physics*. World Scientific, 1989.
- [35] Kenneth G. Wilson. Confinement of quarks. *Phys. Rev. D*, 10:2445–2459, Oct 1974.
- [36] Seiji Sugawa, Francisco Salces-Carcoba, Yuchen Yue, Andika Putra, and Ian B. Spielman. Wilson loop and Wilczek–Zee phase from a non-Abelian gauge field. *npj Quantum Information*, 7(144), 2021.
- [37] Frank Wilczek and Alfred D Shapere. *Geometric phases in physics*. Advanced series in mathematical physics. World Scientific, Singapore, 1989.
- [38] Weichao Yu, Tao Yu, and Gerrit E. W. Bauer. Circulating cavity magnon polaritons. *Phys. Rev. B*, 102:064416, Aug 2020.
- [39] Ana Lopez Moran, Juan Córcoles, Jorge Ruiz-Cruz, José Montejo-Garai, and Jesus Rebolgar. Electromagnetic scattering at the waveguide step between equilateral triangular waveguides. *Advances in Mathematical Physics*, 2016:1–16, 01 2016.
- [40] Yuntian Chen, Ruo-Yang Zhang, Zhongfei Xiong, Zhi Hong Hang, Jensen Li, Jian Qi Shen, and C. T. Chan. Non-Abelian gauge field optics. *Nature Communications*, 10:3125, July 2019.
- [41] Kyrlyo Snizhko, Reinhold Egger, and Yuval Gefen. Non-Abelian Berry phase for open quantum systems: Topological protection versus geometric dephasing. *Phys. Rev. B*, 100:085303, Aug 2019.
- [42] Y. N. Zhang, J. Shen, H. D. Liu, and X. X. Yi. Non-Abelian quantum adiabatic dynamics and phase simulation with classical resonant oscillators. *Phys. Rev. A*, 102:032213, Sep 2020.
- [43] Yang Liu, Y. N. Zhang, X. X. Yi, and H. D. Liu. Non-Abelian phase and geometric force in a quantum-classical hybrid system. *Phys. Rev. A*, 109:052203, May 2024.
- [44] P.-Y. Bourgeois and V. Giordano. Simple model for the mode-splitting effect in whispering-gallery-mode resonators. *IEEE Transactions on Microwave Theory and Techniques*, 53(10):3185–3190, 2005.
- [45] Luca Visinelli. Axion-electromagnetic waves. *Modern Physics Letters A*, 28(35):1350162, 2013.
- [46] David M. Pozar. *Rectangular Waveguide Cavity Resonators*, page 284–285. J. Wiley & Sons, 4 edition, 2012.

## SUPPLEMENTARY MATERIAL

### S1. Derivation of the Non-Abelian Berry Phase Formula

In this section, we derive the expression for  $\Pi_{(n,j)}$  in a  $D_3^{r \neq 0} A$  resonator using the non-Abelian holonomy (Wilson loop) formalism introduced by Wilczek and Zee [33], and matrix-valued gauge connections [34–36].

#### A. Mode Structure and Composite Subspaces

As discussed in the main text, for each azimuthal index  $n$ , the  $\text{TE}_{1,0,n}$  family supports two non-degenerate solutions corresponding to opposite  $\mathcal{H}_n$  sectors.

Each  $\mathcal{H}_n$  sector ( $\pm$ ) supports a pair of degenerate modes whose azimuthal field distributions exhibit  $\cos(n\theta)$  and  $\sin(n\theta)$  angular dependence, and which transform under the 2D  $E$  irreducible representation of the  $D_3$  point group. To capture these two independent internal degrees of freedom, the full mode manifold is described by a direct-product structure  $\mathbb{C}^2 \otimes \mathbb{C}^2$ . These 2D subspaces are encoded by the following complex local-amplitude state vectors parameterised by arclength  $s$ ,

$$|u(s)\rangle = \begin{pmatrix} u_1(s) \\ u_2(s) \end{pmatrix}, \quad |r(s)\rangle = \begin{pmatrix} r_1(s) \\ r_2(s) \end{pmatrix}. \quad (\text{S.1})$$

The total four-component local state is therefore

$$|\Psi(s)\rangle = |u(s)\rangle \otimes |r(s)\rangle, \quad \langle \Psi(s) | \Psi(s) \rangle = 1, \quad (\text{S.2})$$

$$|\Psi(s)\rangle = \begin{pmatrix} u_1(s) r_1(s) \\ u_1(s) r_2(s) \\ u_2(s) r_1(s) \\ u_2(s) r_2(s) \end{pmatrix},$$

which forms the basis for describing adiabatic parallel transport along the twisted cavity.

#### B. Wilczek–Zee Non-Abelian Berry Connection

The Wilczek–Zee non-Abelian gauge connection acting on  $|\Psi(s)\rangle$  is [33, 36]

$$A_s^{\alpha\beta} = i \langle \Psi_\alpha(s) | \partial_s \Psi_\beta(s) \rangle, \quad \alpha, \beta \in \{1, 2, 3, 4\}, \quad (\text{S.3})$$

where  $A_s$  is a  $4 \times 4$  matrix-valued gauge potential acting on the degenerate internal mode subspace.

#### C. Holonomy (Wilson Loop)

Adiabatic evolution around a closed loop  $C$  results in the accumulated parallel transport of the degenerate mode subspace, producing the non-Abelian holonomy (Wilson loop) [33, 36, 37]:

$$U = \mathcal{P} \exp \left( i \oint_C A_s ds \right), \quad (\text{S.4})$$

where  $\mathcal{P}$  denotes path ordering, required when  $[A_s(s), A_s(s')] \neq 0$  along the trajectory, reflecting the non-Abelian nature of the gauge field. Since  $A_s$  is Hermitian, the resulting holonomy  $U$  is unitary ( $U^\dagger = U^{-1}$ ). Diagonalising  $U$  yields the observable eigenphases, which correspond to the physically measurable phase shifts:

$$U |\psi_j\rangle = e^{i\Pi_{(n,j)}} |\psi_j\rangle, \quad j \in \{1, 2, 3, 4\}. \quad (\text{S.5})$$

#### D. Resonant Mode Condition

After propagation through half of the cavity (at arclength  $s = L/2$ ), the CW and CCW travelling-wave components are

$$|\psi_{\text{CW}}\rangle = e^{+i\phi_d} U_{1/2} |\Psi(0)\rangle, \quad (\text{S.6})$$

$$|\psi_{\text{CCW}}\rangle = e^{-i\phi_d} U_{1/2}^{-1} |\Psi(0)\rangle, \quad (\text{S.7})$$

where  $U_{1/2}$  is the segment holonomy, describing the geometric evolution of the degenerate internal mode subspace over a half-round trip of the cavity. The full holonomy is  $U = U_{1/2}^{(2)} U_{1/2}^{(1)}$ . The scalar dynamical phase accumulated over this half-round trip is [3]

$$\phi_d = n_{\text{eff}} k R \pi, \quad (\text{S.8})$$

where  $n_{\text{eff}}$  is the effective refractive index and  $k$  is the wavenumber.

The normalised standing-wave superpositions of the CW and CCW travelling-wave components are

$$|\psi_{\text{cos}}\rangle = \frac{1}{\sqrt{2}} (|\psi_{\text{CW}}\rangle + |\psi_{\text{CCW}}\rangle), \quad (\text{S.9})$$

$$|\psi_{\text{sin}}\rangle = \frac{i}{\sqrt{2}} (|\psi_{\text{CW}}\rangle - |\psi_{\text{CCW}}\rangle). \quad (\text{S.10})$$

Using  $U_{1/2}^\dagger = U_{1/2}^{-1}$  (since  $U$  is unitary), the associated

amplitude for the  $|\psi_{\text{cos}}\rangle$  is

$$\begin{aligned} A_{\text{cos}} &= \langle \psi_{\text{cos}} | \psi_{\text{cos}} \rangle, \\ &= 1 + \frac{1}{2} e^{2i\phi_d} \langle \Psi(0) | U | \Psi(0) \rangle \\ &\quad + \frac{1}{2} e^{-2i\phi_d} \langle \Psi(0) | U^{-1} | \Psi(0) \rangle, \end{aligned} \quad (\text{S.11})$$

and for  $|\psi_{\text{sin}}\rangle$  is

$$\begin{aligned} A_{\text{sin}} &= \langle \psi_{\text{sin}} | \psi_{\text{sin}} \rangle, \\ &= 1 - \frac{1}{2} e^{2i\phi_d} \langle \Psi(0) | U | \Psi(0) \rangle \\ &\quad - \frac{1}{2} e^{-2i\phi_d} \langle \Psi(0) | U^{-1} | \Psi(0) \rangle. \end{aligned} \quad (\text{S.12})$$

Expanding  $|\Psi(0)\rangle$  in the eigenbasis of  $U$ ,

$$|\Psi(0)\rangle = \sum_j c_j |\psi_j\rangle, \quad \sum_j |c_j|^2 = 1, \quad (\text{S.13})$$

and using the orthonormality relation  $\langle \psi_{j'} | \psi_j \rangle = \delta_{j'j}$ , the expression in (S.11) becomes

$$\begin{aligned} A_{\text{cos}} &= 1 + \frac{1}{2} e^{i2\phi_d} \sum_{j=1}^4 |c_j|^2 e^{i\Pi(n,j)} \\ &\quad + \frac{1}{2} e^{-i2\phi_d} \sum_{j=1}^4 |c_j|^2 e^{-i\Pi(n,j)}, \\ &= 1 + \sum_{j=1}^4 |c_j|^2 \cos(2\phi_d + \Pi(n,j)), \end{aligned} \quad (\text{S.14})$$

and similarly, (S.12) reduces to

$$\begin{aligned} A_{\text{sin}} &= 1 - \frac{1}{2} e^{i2\phi_d} \sum_{j=1}^4 |c_j|^2 e^{i\Pi(n,j)} \\ &\quad - \frac{1}{2} e^{-i2\phi_d} \sum_{j=1}^4 |c_j|^2 e^{-i\Pi(n,j)}, \\ &= 1 - \sum_{j=1}^4 |c_j|^2 \cos(2\phi_d + \Pi(n,j)). \end{aligned} \quad (\text{S.15})$$

Resonance occurs at the maxima of  $A_{\text{cos}}$  and  $A_{\text{sin}}$ . Using (S.8), this gives

$$\boxed{2n_{\text{eff}} k R \pi + \Pi(n,j) = 2\pi n}, \quad (\text{S.16})$$

and

$$\boxed{2n_{\text{eff}} k R \pi + \Pi(n,j) = \pi(2n+1)}. \quad (\text{S.17})$$

For the  $D_{3S}^r$  resonator, CW and CCW traverse identical paths due to the cavity's mirror symmetry; the holonomy reduces to  $U = \mathbb{1}$  and no  $\Pi(n,j)$  is accumulated. The corresponding resonant mode conditions are therefore

$$2n_{\text{eff}} k_{(n,j)}^S R \pi = 2\pi n, \quad (\text{S.18})$$

$$2n_{\text{eff}} k_{(n,j)}^S R \pi = \pi(2n+1), \quad (\text{S.19})$$

where  $k_{(n,j)}^S$  is the wavenumber of the  $\text{TE}_{1,0,(n,j)}$  mode in the symmetric resonator.

For the  $D_{3A}^{r \neq 0}$  resonator, the twist breaks this symmetry, and therefore  $\Pi(n,j)$  must be included in the resonance condition:

$$2n_{\text{eff}} k_{n+\Delta n}^A R \pi + \Pi(n,j) = 2\pi n, \quad (\text{S.20})$$

$$2n_{\text{eff}} k_{n+\Delta n}^A R \pi + \Pi(n,j) = \pi(2n+1), \quad (\text{S.21})$$

where  $k_{n+\Delta n}^A$  is the wavenumber of the  $\text{TE}_{1,0,n+\Delta n}$  mode in the asymmetric resonator.

### E. Deriving The Non-Abelian Eigenphases

Comparing (S.18) with (S.20), and (S.19) with (S.21), at fixed  $n$ , yields the phase shift acquired in each eigenchannel  $j$  of the  $D_{3A}^{r \neq 0}$  resonator due to the geometric twist:

$$\Pi(n,j) = 2n_{\text{eff}} R \pi \delta k \quad \delta k \equiv k_n^S - k_{n+\Delta n}^A. \quad (\text{S.22})$$

Because the  $\text{TE}_{1,0,n+\Delta n}$  and  $\text{TE}_{1,0,n}$  doublets follow the same modal spectrum [see Fig. 3(c)], the wavenumber difference,  $\delta k$ , relates to the experimentally measured frequency shift  $\Delta f_n = f_n^S - f_{n+\Delta n}^A$ . Using the group velocity,  $V_g = \delta\omega/\delta k$ , with  $\delta\omega = 2\pi\Delta f_n$  and  $n_{\text{eff}} = 1$  (vacuum), (S.22) becomes

$$\boxed{\Pi(n,j) = \Delta f_{(n,j)} \frac{4\pi^2 R}{V_g}}. \quad (\text{S.23})$$

### F. Group Velocity

For electromagnetic waves in a waveguide,  $V_g$  relates to the phase velocity  $V_p$  by [38]

$$V_g = \frac{c^2}{V_p}, \quad (\text{S.24})$$

with

$$V_p = \frac{2\pi f_n}{\sqrt{k^2 - k_{cp}^2}}, \quad (\text{S.25})$$

where  $k_{cp}$  is the cutoff wavenumber for a particular mode family, which in a  $D_3$  waveguide is [39]

$$k_{cp} = \frac{4\pi}{3v} \sqrt{m^2 + p^2 + mp}. \quad (\text{S.26})$$

For the  $\text{TE}_{1,0,n}$  modes this gives  $k_{cp} = \frac{4\pi}{3v}$ . Substituting  $k_{cp}$  into (S.25) and using  $k = c/\omega$  with (S.24) yields  $V_g$  for the  $\text{TE}_{1,0,n}$  modes in the  $D_3$  resonator:

$$V_g = c \sqrt{1 - \left( \frac{2c}{3v f_n^S} \right)^2}. \quad (\text{S.27})$$

Since the  $D_3^{r \neq 0}_A$  resonator has the same transverse cross-section as the  $D_3^S$  resonator, they share the same  $V_g$  expression.

### G. Experimental Formula For the Non-Abelian Eigenphases

Substituting (S.27) into (S.23) gives the working experimental formula

$$\Pi_{(n,j)} = \Delta f_{(n,j)} \frac{4\pi^2 R}{c \sqrt{1 - \left( \frac{2c}{3v f_{(n,j)}^S} \right)^2}}. \quad (\text{S.28})$$

## S2. Analytical Formula for the Non-Abelian Berry Phases

We now compute  $\Pi_{(n,j)}$  analytically, similar to that done in other studies such as in non-Abelian gauge optics [40–43]. The two counter-propagating solutions are described by complex amplitudes  $a_+(\theta)$  and  $a_-(\theta)$ .

Transforming to standing-wave components gives [44]

$$V(\theta) = \frac{a_+(\theta) + a_-(\theta)}{\sqrt{2}} = \cos(n\theta), \quad (\text{S.29})$$

$$I(\theta) = \frac{a_+(\theta) - a_-(\theta)}{\sqrt{2}} = \sin(n\theta). \quad (\text{S.30})$$

Thus the initial internal mode-amplitude vectors at  $s = 0$ , corresponding to the azimuthal angle  $\theta$ , are

$$|u(0)\rangle = \begin{pmatrix} \psi_1 \\ \psi_2 \end{pmatrix}, \quad |r(0)\rangle = \begin{pmatrix} \cos(n\theta) \\ \sin(n\theta) \end{pmatrix}. \quad (\text{S.31})$$

The total initial local field state is therefore expressed as the direct-product form

$$|\Psi(0)\rangle = \begin{pmatrix} \psi_1 \cos(n\theta) \\ \psi_1 \sin(n\theta) \\ \psi_2 \cos(n\theta) \\ \psi_2 \sin(n\theta) \end{pmatrix}. \quad (\text{S.32})$$

The modal amplitudes  $|u(s)\rangle$  evolve adiabatically with the slow geometric rotation of the resonator walls, parametrised by  $\alpha(s)$ . Their transport is given by the electromagnetic duality rotation [25, 26, 45]

$$R[\alpha(s)] = \begin{pmatrix} \cos \alpha(s) & \sin \alpha(s) \\ -\sin \alpha(s) & \cos \alpha(s) \end{pmatrix}, \quad R^\dagger R = I, \quad (\text{S.33})$$

so that

$$|u(s)\rangle = R[\alpha(s)] |u(0)\rangle. \quad (\text{S.34})$$

Backscattering due to perturbations (e.g. surface defects, machining imperfections) couples the CW and CCW components. We model this by an equivalent transmission-line loop with a normalised shunt reactance  $i x[\alpha(s)]$  [44], which yields the transmission and reflection coefficients

$$T[\alpha(s)] = \frac{2i x[\alpha(s)]}{1 + 2i x[\alpha(s)]}, \quad (\text{S.35})$$

$$\Gamma[\alpha(s)] = \frac{-1}{1 + 2i x[\alpha(s)]}. \quad (\text{S.36})$$

The corresponding backscattering transformation is

$$B[\alpha(s)] = \begin{pmatrix} T[\alpha(s)] & \Gamma[\alpha(s)] \\ \Gamma[\alpha(s)] & T[\alpha(s)] \end{pmatrix}, \quad B^\dagger B = I, \quad (\text{S.37})$$

and the CW/CCW amplitudes evolve as

$$|r(s)\rangle = B[\alpha(s)] |r(0)\rangle. \quad (\text{S.38})$$

The resulting evolution of the 4-component field state is

$$|\Psi(s)\rangle = K[\alpha(s)] |\Psi(0)\rangle \quad (\text{S.39})$$

where

$$\begin{aligned} K[\alpha(s)] &= R[\alpha(s)] \otimes B[\alpha(s)] \\ &= \begin{pmatrix} T \cos \alpha & \Gamma \cos \alpha & T \sin \alpha & \Gamma \sin \alpha \\ \Gamma \cos \alpha & T \cos \alpha & \Gamma \sin \alpha & T \sin \alpha \\ -T \sin \alpha & -\Gamma \sin \alpha & T \cos \alpha & \Gamma \cos \alpha \\ -\Gamma \sin \alpha & -T \sin \alpha & \Gamma \cos \alpha & T \cos \alpha \end{pmatrix}. \end{aligned} \quad (\text{S.40})$$

Differentiating (S.39) with respect to  $s$  gives

$$\partial_s |\Psi(s)\rangle = \frac{d\alpha}{ds} J |\Psi(s)\rangle, \quad (\text{S.41})$$

where

$$J \equiv \frac{dK}{d\alpha} K^{-1}. \quad (\text{S.42})$$

Thus substituting (S.41) into (S.3) gives

$$A_s = i \frac{d\alpha}{ds} J, \quad (\text{S.43})$$

and the holonomy over a path segment (S.4) with total director rotation  $\Delta\alpha = \int_C d\alpha$  is then

$$U = \exp\left(-\int_C \frac{d\alpha}{ds} J ds\right). \quad (\text{S.44})$$

We now examine how the non-Abelian phases  $\Pi_{(n,j)}$  behave under different classes of backscattering perturbations.

#### A. Uniform discontinuity over the rotation $\alpha(s)$

We first consider a perturbation that is uniform over the full director rotation  $\alpha(s)$ . The corresponding transmission and reflection coefficients  $T$  and  $\Gamma$  are plotted in Fig. S1. Panels (a)-(b) show the response for a weak perturbation ( $x \gg 1$ ; here  $x = 10^6$ ), while panels (c)-(d) show the behaviour under a stronger macroscopic perturbation ( $x = 0.1$ ).

In this case, it turns out that (S.42) evaluates to a

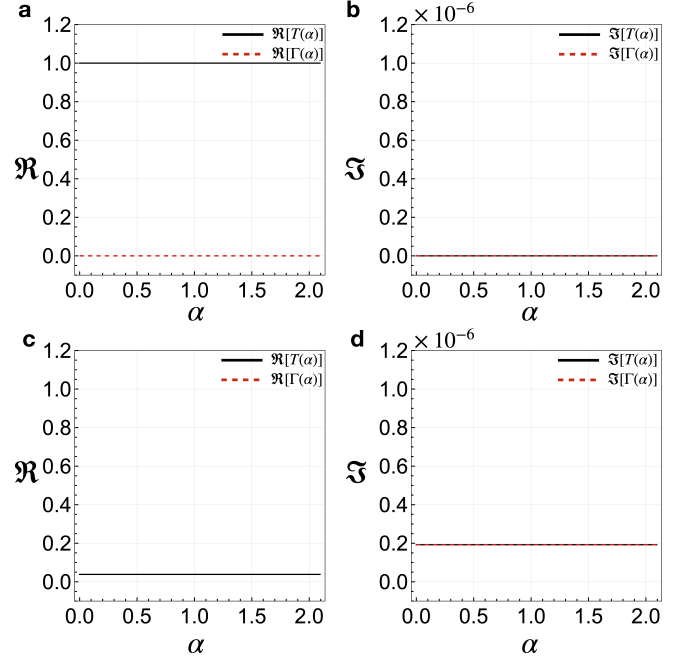


Figure S1. Real (a,c) and imaginary (b,d) parts of the coefficients  $T$  and  $\Gamma$ , respectively, for a uniform discontinuity along the rotation  $\alpha(s)$  in the  $D_3^{r \neq 0} A$  resonator. Panels (a,b) show a weak perturbation ( $x = 10^6$ ), while panels (c,d) show a stronger perturbation ( $x = 0.1$ ).

constant that is independent of the perturbation strength  $x$ . This matrix is

$$J[\alpha(s)] = \begin{pmatrix} 0 & 0 & 1 & 0 \\ 0 & 0 & 0 & 1 \\ -1 & 0 & 0 & 0 \\ 0 & -1 & 0 & 0 \end{pmatrix}. \quad (\text{S.45})$$

Because  $J[\alpha(s)]$  is constant, (S.44) can be evaluated as

$$\begin{aligned} U &= \exp\left(-J \int_C d\alpha\right), \\ &= \exp(-J \Delta\alpha). \end{aligned} \quad (\text{S.46})$$

Here  $\Delta\alpha$  is equivalent to the twist of the  $D_3^{r \neq 0} A$  resonator, which is given by  $\Delta\alpha = \frac{2\pi r}{3}$  for integer twist number  $r$ .

Diagonalising  $J$  yields internal mode eigenvectors  $|v_j\rangle$  satisfying

$$J |v_j\rangle = \lambda_j |v_j\rangle, \quad (\text{S.47})$$

with eigenvalues

$$\lambda_j = \{i, i, -i, -i\}. \quad (\text{S.48})$$

Using  $U = e^{-J\Delta\alpha}$ , the associated  $\Pi_{(n,j)}$  are

$$\boxed{\Pi_{n,1} = \Pi_{n,2} = -\Delta\alpha, \quad \Pi_{n,3} = \Pi_{n,4} = +\Delta\alpha}. \quad (\text{S.49})$$

The corresponding eigenvectors are obtained as the columns of

$$V = \begin{pmatrix} 0 & -i & 0 & i \\ -i & 0 & i & 0 \\ 0 & 1 & 0 & 1 \\ 1 & 0 & 1 & 0 \end{pmatrix}, \quad |v_j\rangle = \frac{1}{\sqrt{2}}V_j, \quad (\text{S.50})$$

so that

$$J = V \text{diag}(i, i, -i, -i) V^{-1}. \quad (\text{S.51})$$

Expressed in the physical basis (S.32), the normalized eigenmodes are

$$|v_1\rangle = \frac{1}{\sqrt{2}}(-i\psi_1 + \psi_2)\sin(n\theta), \quad (\lambda_1 = +i), \quad (\text{S.52})$$

$$|v_2\rangle = \frac{1}{\sqrt{2}}(-i\psi_1 + \psi_2)\cos(n\theta), \quad (\lambda_2 = +i), \quad (\text{S.53})$$

$$|v_3\rangle = \frac{1}{\sqrt{2}}(i\psi_1 + \psi_2)\sin(n\theta), \quad (\lambda_3 = -i), \quad (\text{S.54})$$

$$|v_4\rangle = \frac{1}{\sqrt{2}}(i\psi_1 + \psi_2)\cos(n\theta), \quad (\lambda_4 = -i), \quad (\text{S.55})$$

Here,  $\frac{1}{\sqrt{2}}(-i\psi_1 + \psi_2)$  corresponds to the negative- $\mathcal{H}_n$  sector and  $\frac{1}{\sqrt{2}}(i\psi_1 + \psi_2)$  to the positive- $\mathcal{H}_n$  sector. Consequently,  $\{v_1, v_2\}$  form the negative- $\mathcal{H}_n$  doublet and  $\{v_3, v_4\}$  form the positive- $\mathcal{H}_n$  doublet. Within each  $\mathcal{H}_n$  sector, the  $\sin(n\theta)$  and  $\cos(n\theta)$  components remain degenerate and acquire the same  $\Pi_{(n,j)}$ . Modes of opposite  $\mathcal{H}_n$  therefore accumulate equal-magnitude phases of opposite sign.

### B. Infinitesimally Localised Perturbation

We now consider a perturbation that is infinitesimally localised at a single angular position  $\alpha(s) = \alpha_0$ . In this

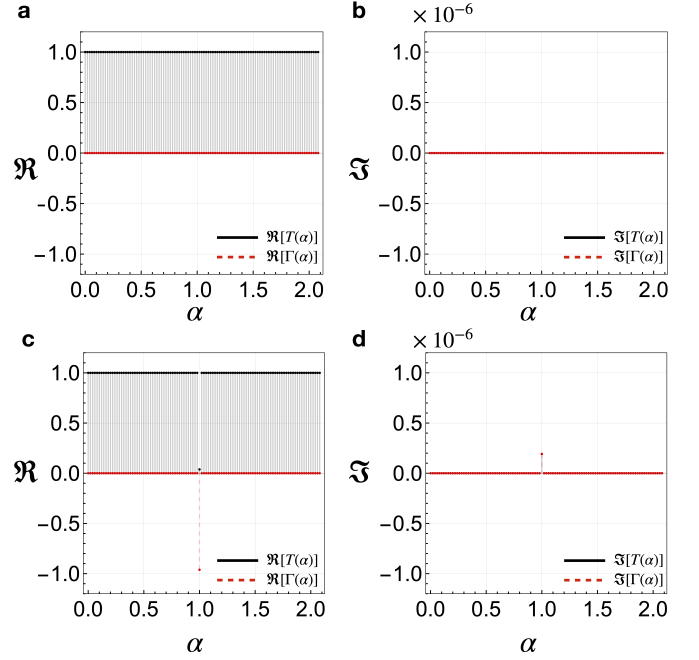


Figure S2. Real (a,c) and imaginary (b,d) parts of the coefficients  $T$  and  $\Gamma$  for an infinitesimally localised perturbation in the  $D_3^{r \neq 0}_A$  resonator. Panels (a,b) show the weak-perturbation case ( $x_1 \rightarrow 300$ ), while panels (c,d) show the strong-perturbation case ( $x_1 \rightarrow 0.1$ ), as a function of the rotation  $\alpha(s)$ .

case, the normalised reactance is modelled as

$$x[\alpha] = x_1 \delta_{\alpha, \alpha_0} + x_0 (1 - \delta_{\alpha, \alpha_0}), \quad x_0 \rightarrow \infty, \quad (\text{S.56})$$

so that the system is unperturbed everywhere except at  $\alpha_0$ , where the perturbation strength is  $x_1$ .

A weak perturbation corresponds to  $x_1 \gg 1$ , with the associated  $T$  and  $\Gamma$  shown in Fig. S2(a) and (b), respectively. A strong, macroscopic perturbation ( $x_1 = 0.1$ ) yields the coefficients plotted in Fig. S2(c) and (d), respectively.

It turns out that  $J[\alpha(s)]$  remains identical to the constant matrix (S.45) in the uniform-perturbation case. Consequently, the expressions in (S.46)-(S.55) still hold without modification. The non-Abelian phases  $\Pi_{(n,j)}$  therefore match those obtained for a uniform perturbation and are independent of the perturbation strength  $x_1$ .

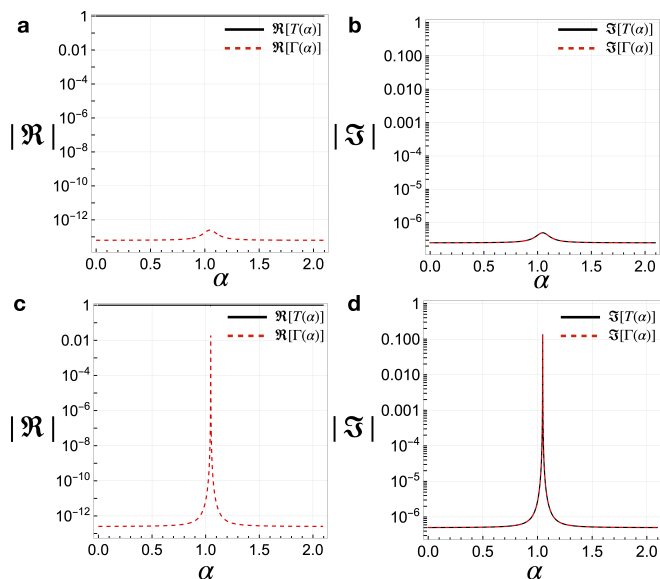


Figure S3. Real (a,c) and imaginary (b,d) parts of  $T$  and  $\Gamma$  for a smoothly localised perturbation in the  $D_3^{r \neq 0}{}_A$  resonator. Panels (a,b) show the weak-perturbation case ( $x_1 \rightarrow 10^6$ ); panels (c,d) show the strong-perturbation case ( $x_1 = 0.1$ ), plotted against the rotation  $\alpha(s)$ .

### C. Smoothly Localised Perturbation

We now consider a perturbation that remains smooth along the full director rotation but is concentrated around a single angular position  $\alpha_0$ . In this case, the normalised reactance is modelled as

$$x[\alpha] = \frac{x_0}{2} \left( 1 + \frac{1 - b(\alpha - \alpha_0)^{-2}}{1 + b(\alpha - \alpha_0)^{-2}} \right) + x_1. \quad (\text{S.57})$$

This functional form introduces a smooth, spatially localised variation in the reactance centred at  $\alpha_0$ , with the parameter  $b$  controlling the width of the perturbation.

A weak perturbation corresponds to  $x_1 \gg 1$ , with the associated coefficients  $T$  and  $\Gamma$  shown in Fig. S3(a) and (b), respectively. A strong perturbation ( $x_1 = 0.1$ ) yields the coefficients plotted in Fig. S3(c) and (d), respectively. In all cases we use  $x_0 = 10^6$ ,  $\alpha_0 = \pi/3$ , and  $b = 0.01$ .

For the weak-perturbation regime, all modifications to the uniform-perturbation matrix in (S.45) are negligible; and (S.46)–(S.55) continue to hold without modification. For the strong perturbation  $x_1 = 0.1$ , evaluating (S.44)

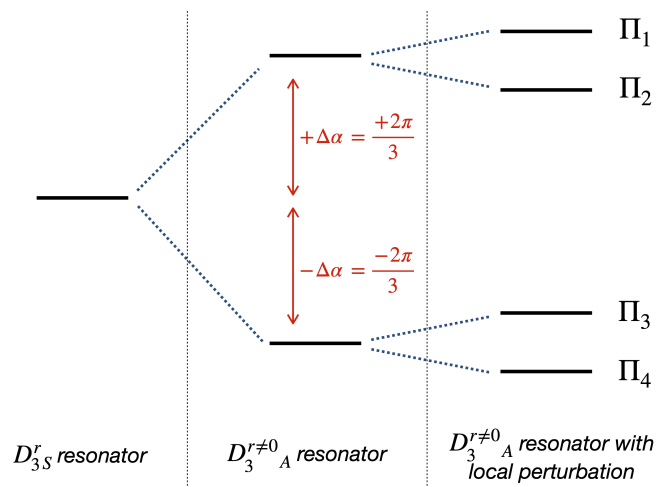


Figure S4. Schematic of the  $\Pi_{(n,j)}$  eigenphase levels for three geometries: the mirror-symmetric  $D_{3S}^r$  resonator, the twisted  $D_3^{r \neq 0}{}_A$  resonator, and the  $D_3^{r \neq 0}{}_A$  resonator with a smoothly localised perturbation centred at the angular position  $\alpha_0$  along the director's full rotation.

numerically for a  $D_{3A}^1$  resonator yields

$$\begin{aligned} \Pi_{n,1} &= 3.79, & \Pi_{n,2} &= 2.95, \\ \Pi_{n,3} &= -1.16, & \Pi_{n,4} &= -0.31, \end{aligned} \quad (\text{S.58})$$

and, expressed in the physical basis (S.32), the normalised eigenmodes remain those of (S.52)–(S.55).

Therefore, under the strong perturbation ( $x_1 = 0.1$ ), the eigenphase spectrum splits into four non-degenerate values, as shown in Fig. S4. This splitting of the previously degenerate eigenphase pairs provides clear evidence that the holonomy acting on the internal mode manifold is intrinsically non-Abelian.

### D. Comparison with Experimental Results

The experimentally measured  $\Pi_{(n,j)}$  values reported in the main paper are consistent with (S.28). This agreement arises because any perturbation present is weak ( $x_1 \gg 1$ ), such that the  $\sin(n\theta)$  and  $\cos(n\theta)$  modes remain effectively frequency-degenerate within the resolution set by the resonator's Q-factor. Modes of opposite  $\mathcal{H}_n$  therefore accumulate equal-magnitude phases of opposite sign, in agreement with the experimental observations presented in the main text.

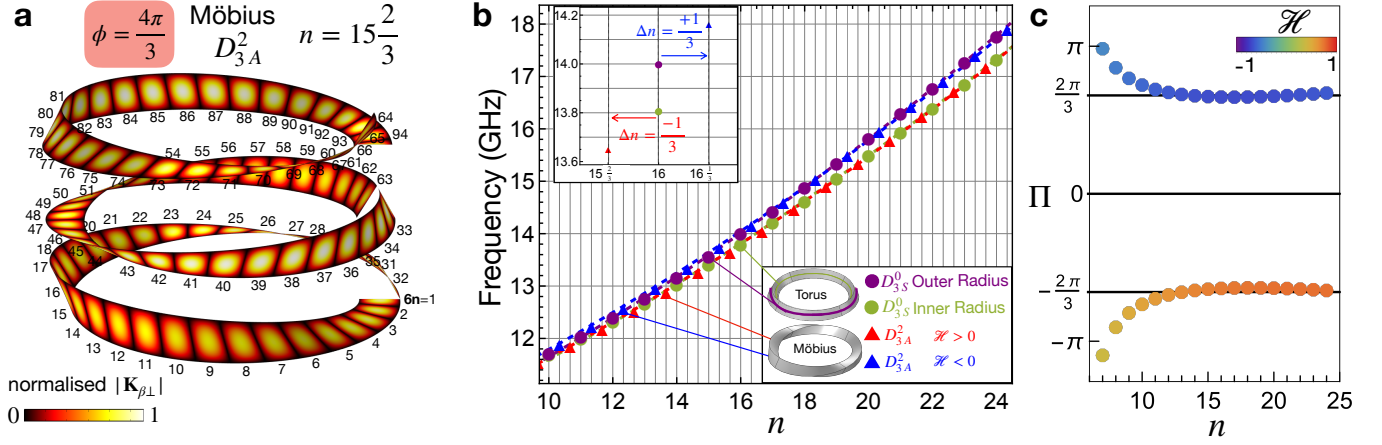


Figure S5. (a) The surface plots of  $|\mathbf{K}_{\beta\perp}|$  for one surface of the FEM simulated  $\text{TE}_{1,0,15\frac{2}{3}}$  mode in the  $D_{3A}^2$  resonator with dimensions of  $v = 19.87$  mm and  $R = 79.58$  mm, with the number of antinodes  $6n$  shown. (b) The modal spectrum of the  $\text{TE}_{1,0,n}$  modes as a function of  $n$  for the  $D_{3A}^2$  and  $D_{3S}^0$  resonators. (c)  $\Pi_{(n,j)}$  as a function of  $n$  with associated  $\mathcal{H}_n$  depicted by colour, where the asymptotic limits are illustrated as black dashed gridlines.

### S3. $D_{3A}^2$ and $D_{3A}^3$ resonators

Fig. S5(a) shows the  $|\mathbf{K}_{\beta\perp}|$  surface plot for the  $\text{TE}_{1,0,15\frac{2}{3}}$  mode in the  $D_{3A}^2$  resonator. The appearance of one-third-integer modes shows that the counter-propagating waves interfere with a  $\frac{2\pi}{3}$  phase offset after one circulation, consistent with spin-redirected Berry phases.

In the case of the  $D_{3A}^2$  resonator,  $\Delta n$  is positive for the  $\mathcal{H}_n < 0$   $\text{TE}_{1,0,n}$  modes and negative for the  $\mathcal{H}_n > 0$   $\text{TE}_{1,0,n}$  modes, as shown in Fig. S5(b). This results in  $\Pi_{(n,j)}$  values equal in magnitude to those of the  $D_{3A}^1$  resonator, but with opposite signs for the  $\mathcal{H}_n > 0$  and  $\mathcal{H}_n < 0$   $\text{TE}_{1,0,n}$  modes, respectively, as shown in Fig. S5(c).

In the case of the  $D_{3A}^3$  resonator, the modes undergo a  $2\pi$  rotation after completing one full circulation of the cavity. This results in their in-phase interference, meaning no  $\Pi_{(n,j)}$  is accumulated. An example of this is shown in Fig. S6(a), where the  $|\mathbf{K}_{\beta\perp}|$  surface plot of the  $\text{TE}_{1,0,16}$  mode exhibits the integer mode number  $n = 16$ . Furthermore, the modal spectrum (see Fig. S6(b)) shows that no shift in  $n$  is required to align the frequencies of the  $D_{3A}^3$  and  $D_{3S}^0$  resonators. Consequently, as confirmed in Fig. S6(c), no  $\Pi_{(n,j)}$  is generated.

### S4. Experimental Mode Assignment Methodology

To verify that the measured resonances correspond to  $\text{TE}_{1,0,n}$  modes, we performed selective excitation using a magnetic loop probe placed at  $\phi = \frac{5\pi}{6}$ , as illustrated in Fig. 1(a) and 6. This probe couples directly to  $H_\phi$ . Rotating the probe by  $90^\circ$  suppresses coupling to  $H_\phi$  and instead enables coupling to  $H_r$ . The corresponding reflection spectra ( $S_{22}$ ) for the two probe orientations are shown in Fig. S7. As expected from the  $\text{TE}_{1,0,n}$  field distribution, large absorption of reflected power is observed on resonances that are well coupled to the  $H_\phi$  probe but vanish when it is rotated, confirming the identity of these lowest-order modes as TE. It is therefore a simple exercise to begin counting mode numbers from the lowest frequency mode.

From the modal spectrum shown in Fig. 3(c), the only way for the  $D_{3A}^1$  resonator modes to match the modal spectrum of the corresponding  $D_{3S}^0$  resonator is if they possess fractional mode numbers of  $n = \mathbb{Z} \pm \frac{1}{3}$ . Furthermore, finite element method (FEM) simulations confirm that the  $D_{3A}^1$  resonator supports such  $\frac{1}{3}$  mode numbers, which can be determined unambiguously by counting the number of anti-nodes of the tangential surface current density over a complete loop of the resonator.

These simulation results match the experimental data in a one-to-one correspondence, as demonstrated in Fig. S8. In this plot, the red dashed line represents the theoretical relationship if simulated and experimental frequencies were identical ( $y=x$ ), and the close alignment of the data points confirms the match.

Since in simulation we can label each mode as  $n = \mathbb{Z} \pm \frac{1}{3}$

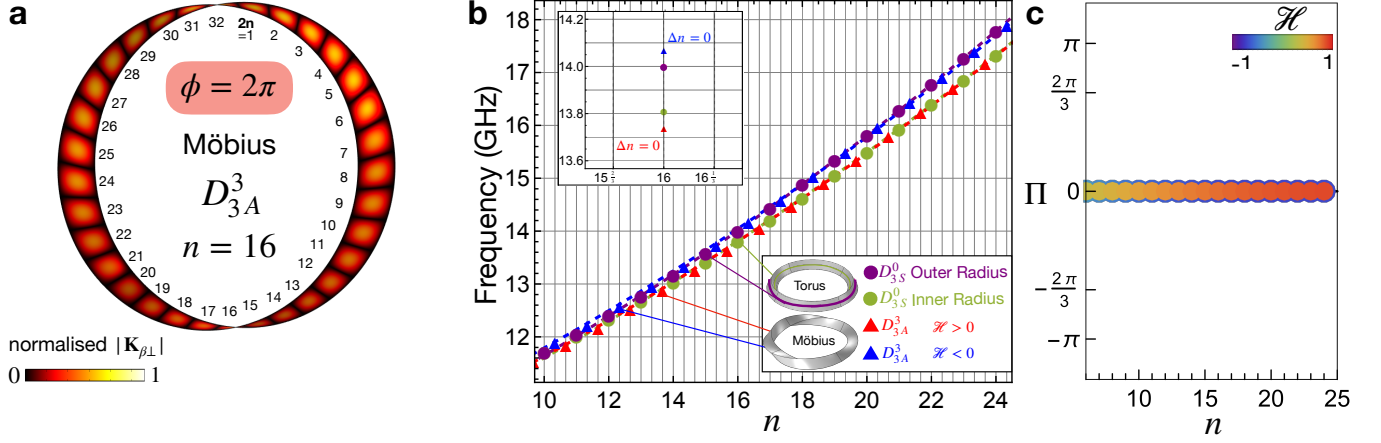


Figure S6. (a) The surface plots of  $|\mathbf{K}_{\beta\perp}|$  for one surface of the FEM simulated  $\text{TE}_{1,0,16}$  mode in the  $D_{3A}^3$  resonator with dimensions of  $v = 19.87$  mm and  $R = 79.58$  mm, with the number of antinodes  $2n$  shown. (b) The modal spectrum of the  $\text{TE}_{1,0,n}$  modes as a function of  $n$  for the  $D_{3A}^3$  and  $D_{3S}^0$  resonators. (c)  $\Pi_{(n,j)}$  as a function of  $n$  with associated  $\mathcal{H}_n$  depicted by colour.

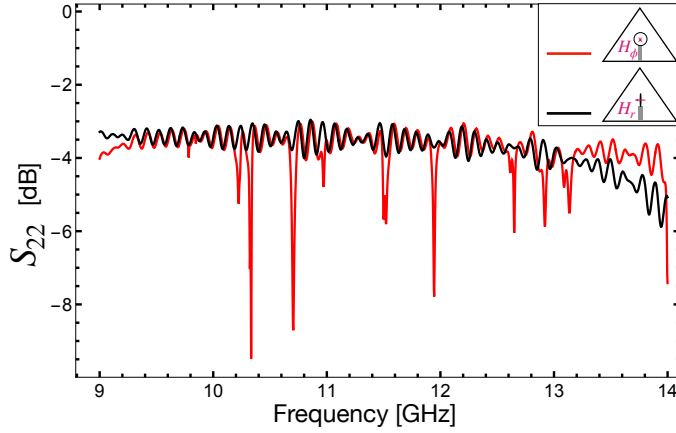


Figure S7. Reflection spectra of the  $R = 23.67$  mm  $D_{3A}^1$  resonator measured with a magnetic loop probe positioned to couple to  $H_{\phi}$  (red) and after a  $90^\circ$  rotation that couples to  $H_r$  (black). The selective excitation confirms the identification of the  $\text{TE}_{1,0,n}$  modes.

starting from the first observed mode, and the simulated frequencies correspond directly to the experimental ones, it follows that the experimental modes can be assigned the same  $\frac{1}{3}$  mode numbers by counting sequentially from the first observed mode. This combined modal spectrum analysis and simulation-to-experiment frequency matching provides an unambiguous method for identifying the fractional mode numbers in the measured spectra.

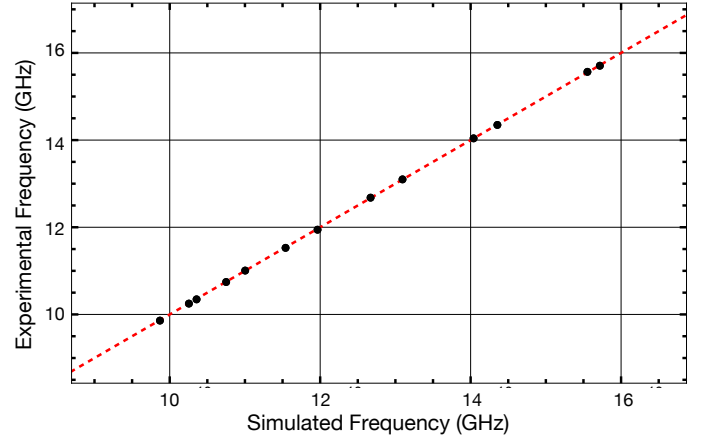


Figure S8. Comparison between simulated and experimental frequencies of the  $R = 23.67$  mm  $D_{3A}^1$  resonator. The red dashed line indicates the theoretical one-to-one correspondence.

### S5. Deriving Berry phase for the $R = 23.67$ mm cavity

The experimental cavity with  $v = 19.92 \pm 0.01$  mm and  $R = 23.67 \pm 0.04$  mm was also simulated using FEM. The eigenfrequencies of both experimentally measured resonant frequencies and the simulated eigenfrequency results are plotted in Fig. S9, along with the fitted frequency dependence of a simulated  $D_{3S}^0$  resonator of the same

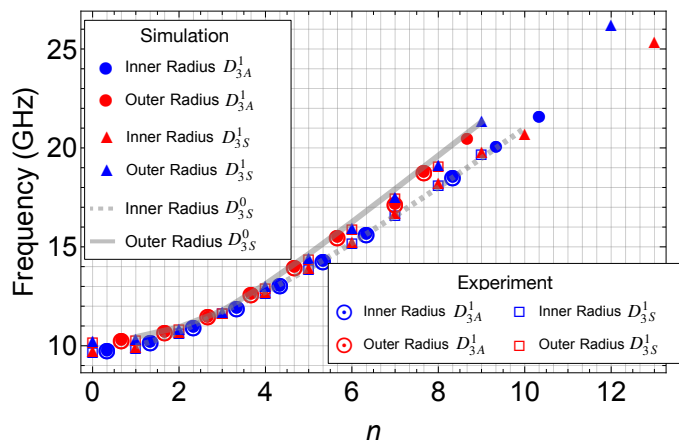


Figure S9. Simulated and experimental eigenfrequencies of the  $R = 23.67$  mm  $D_{3A}^1$  resonator with various twist configurations.

dimensions. We observe excellent agreement between experimental and simulated frequencies, which makes it relatively simple to assign the correct mode numbers to the measured resonant frequencies. Using these frequencies and (S.28), the simulated and experimental  $\Pi_{(n,j)}$  values are derived, as shown in Fig. 5.

### S6. Dependence on cavity radius, $R$

As the cavity radius,  $R$ , of a toroid cavity becomes larger, it behaves more like an ideal waveguide as the curvature of the cavity becomes less pronounced. As such, the free spectral range of the resonant modes becomes more uniform as  $R$  increases. This can be seen from Fig. S10 in which cavity eigenfrequencies for the  $D_{3A}^1$  resonator are plotted as a function of  $R$ .

In the large- $R$  limit, a significantly greater number of  $\text{TE}_{1,0,n}$  modes occur before the onset of higher-order modes compared to the smaller- $R$  case. This provides a broader range of modes free from mode mixing, and thus a wider frequency span over which the ideal  $\Pi_{(n,j)} = s_j \frac{2\pi}{3}$  ( $s_j = -1, -1, +1, +1$ ) is observed. Additionally, the resonant mode spacing becomes more uniform, which makes the  $\Pi_{(n,j)}$  analysis simpler and more reliable.

### S7. Electromagnetic Helicity

Electromagnetic helicity,  $\mathcal{H}$ , can be derived from the projection of the spin angular momentum of a com-

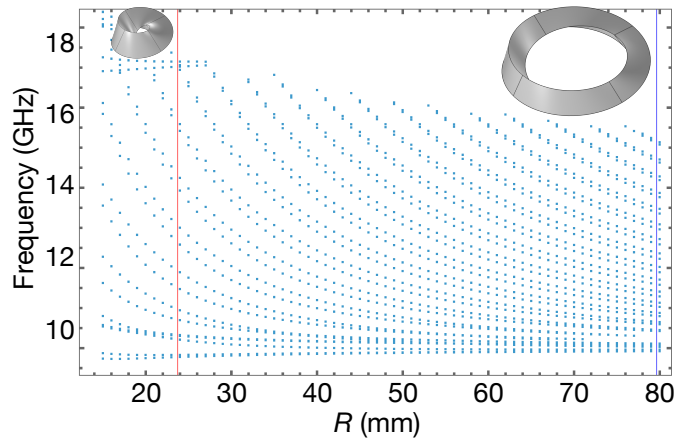


Figure S10. Simulated eigenfrequencies of the  $D_{3A}^1$  resonator as a function of cavity radius  $R$ . Inset and shown in red and blue are the two cavity radii discussed in the main paper,  $R = 23.67$  mm and  $R = 79.58$  mm, respectively. The smaller  $R$  cavity is the dimension of the physical cavity that was manufactured and experimentally tested.

plex electromagnetic field onto its linear momentum vector [19, 25]. The sign of this projection distinguishes between opposite  $\mathcal{H}$  states, and the expectation value of the corresponding operator yields the local, time-averaged helicity density [26–29].

The total resonant  $\mathcal{H}$ , associated with a given monochromatic electromagnetic mode  $n$ , is defined as the volume integral of the helicity density,  $h_n$ , over the cavity volume:

$$\mathcal{H}_n = \int h_n dV. \quad (\text{S.59})$$

The local helicity density,  $h_n$ , is given by

$$\begin{aligned} h_n(\vec{r}) &= 2\text{Im} \left[ \vec{\mathbf{e}}_n(\vec{r}) \cdot \vec{\mathbf{h}}_n^*(\vec{r}) \right], \\ &= \frac{2\text{Im} \left[ \vec{\mathbf{E}}_n(\vec{r}) \cdot \vec{\mathbf{H}}_n^*(\vec{r}) \right]}{V\mathcal{E}\mathcal{H}}. \end{aligned} \quad (\text{S.60})$$

Here,  $\mathcal{E} = \sqrt{\frac{1}{V} \int |\vec{\mathbf{E}}_n(\vec{r})|^2 dV}$  and  $\mathcal{H} = \sqrt{\frac{1}{V} \int |\vec{\mathbf{H}}_n(\vec{r})|^2 dV}$  are real constants,  $\vec{\mathbf{E}}_n(\vec{r}) = \mathcal{E}\vec{\mathbf{e}}_n(\vec{r})$  and  $\vec{\mathbf{H}}_n(\vec{r}) = \mathcal{H}\vec{\mathbf{h}}_n(\vec{r})$  are the electric and magnetic vector fields of the mode, respectively, and  $\vec{\mathbf{e}}_n(\vec{r})$  and  $\vec{\mathbf{h}}_n(\vec{r})$  are the normalised position dependent eigenvectors such that  $\frac{1}{V} \int \vec{\mathbf{e}}_n(\vec{r}) \cdot \vec{\mathbf{e}}_n(\vec{r}) dV = \frac{1}{V} \int \vec{\mathbf{h}}_n(\vec{r})^* \cdot \vec{\mathbf{h}}_n(\vec{r}) dV = 1$ . Equation (S.60) thus provides a pointwise measure of helicity within the resonant mode, while (S.59) captures the net helicity of

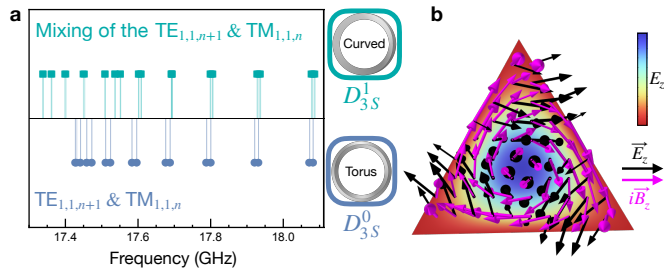


Figure S11. (a) The eigenfrequencies of the higher-order  $\text{TE}_{1,1,n+1}$  and  $\text{TM}_{1,1,n}$  modes in the  $D_{3S}^0$  and  $D_{3S}^1$  resonators of dimensions  $v = 19.87$  mm and  $R = 79.58$  mm. (b) The  $E_z$  field in the cross-section of the  $D_{3S}^1$  resonator for the fundamental helical mode resulting from the mixing of the  $\text{TE}_{1,1,n+1}$  and  $\text{TM}_{1,1,n}$  modes, with the arrows showing the electric vector field  $\vec{E}_z$  (black) and magnetic vector field  $i\vec{H}_z$  (magenta).

the resonant mode.

## S8. Higher-Order Modes of the Möbius Resonator

### A. No Accumulation of Berry Phase

The modes with near-unity  $\mathcal{H}_n$  in the  $D_3^{r \neq 0}$  resonator have rotational symmetry and therefore will always be in phase after one full circulation of the cavity, resulting in no accumulated Berry phase.

### B. Curved vs. Torus Resonator

Unlike the lower-order  $\text{TE}_{1,0,n}$  modes, the higher-order modes don't have equivalent resonant frequency in the  $D_{3S}^0$  and  $D_{3S}^{r \neq 0}$  resonator, as demonstrated in Fig. S11(a). This discrepancy arises due to the curved electrically conducting boundary conditions of the  $D_{3S}^{r \neq 0}$  resonator, which couples the  $\text{TE}_{1,1,n+1}$  and  $\text{TM}_{1,1,n}$  modes, generating resonances with nonzero  $h_n$ . This nonzero  $h_n$  has a frequency-shifting effect on the resonant modes in the  $D_{3S}^r$  resonator compared to the  $D_{3S}^0$  resonator [19, 25]. This coupling effect is visualised in the field plot shown in Fig. S11(b). Note that in the  $D_{3S}^r$  resonator, these modes exhibit zero net  $\mathcal{H}_n$ , as  $h_n$  takes opposite signs at all points on either side of the resonator, resulting in cancellation as it is integrated over the cavity volume.

## S9. $D_2$ (rectangular) resonators

Changing the cross-section of the resonator to be  $D_2$ , the geometries seen in Fig. S12(a) and (b) are constructed for the  $D_{2A}^1$  and  $D_{2S}^1$  forms. In the  $D_{2A}^1$  resonator the wavevector orientation is now rotated by  $\pi$  radians, corresponding to the solid angle it traces out in momentum space [15, 22–24] or in other words, the closed loop of latitude it forms on the Poincaré sphere. Once again, in the following analysis, we focus on the  $\text{TE}_{1,0,n}$  mode family. Only a single Berry phase  $\Pi_n = \pi$  is accumulated in this resonator as a result of the symmetry of its  $D_2$  cross-section. Unlike the  $D_3$  cross-section, whose 2D  $E$  irreducible representation supports an inner-outer surface  $\text{TE}_{1,0,n}$  doublet, the  $D_2$  cross-section possesses only 1D irreducible representation. As a result, it does not generate this inner-outer surface  $\text{TE}_{1,0,n}$  doublet and does not form a 2D subspace on which a matrix-valued non-Abelian holonomy can act. Instead, the geometric phase reduces to a scalar Abelian  $U(1)$   $\Pi_n$ .

The counter-propagating waves that travel around a  $D_{2A}^1$  resonator constructively interfere out of phase forming a standing wave pattern with  $n = \mathbb{Z} + \frac{1}{2}$  number of variations along the axial direction of the resonator [3]. In the case of the  $D_{2S}^1$  resonator, the counter-propagating waves will constructively interfere in phase to form resonant modes with integer mode numbers. The existence of  $n = \mathbb{Z} + \frac{1}{2}$  mode numbers in the  $D_{2A}^1$  resonator thus serves as evidence for the generation of a spin-redirected Berry phase.

To calculate the azimuthal mode number  $n$  of a given resonant mode, the number of anti-nodes in the tangential surface current density  $|\mathbf{K}_\tau|$  is again counted around a complete loop of the resonator. The surface charges in a given cross section, and the associated bulk electric fields are shown in Fig. S12(c), where the electric field of the resonator bulk moves from the negatively charged surface to the positively charged surface. For the purpose of mode counting, we again utilise the azimuthal tangential component of the surface current density,  $\mathbf{K}_{\beta\perp}$ . As before, the number of anti-nodes must be divided by the number of windings and then divided by two to account for  $2n$  anti-nodes in  $2\pi$  radians. The number of windings is two in the case of the  $D_{2A}^1$  resonator and one in the case of the geometrically equivalent  $D_{2S}^1$  resonator.

The FEM simulated  $|\mathbf{K}_{\beta\perp}|$  surface plot of the  $\text{TE}_{1,0,19\frac{1}{2}}$  mode in the  $D_{2A}^1$  resonator is shown in Fig. S12(d). The number of anti-nodes over two windings of the closed loop was  $N = 78$ , giving the mode number  $n = N/4 = 19.5$ . As expected, the  $\text{TE}_{1,0,n}$  modes in the  $D_{2A}^1$  resonator

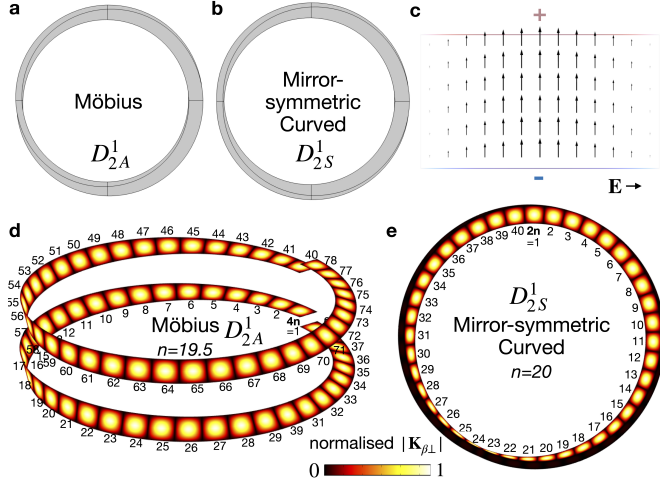


Figure S12. (a) The geometry of the  $D_{2A}^1$  cavity, along with the equivalent (b)  $D_{2S}^1$  cavity. (c) The cross-section of the  $\text{TE}_{1,0,n}$  mode in the FEM simulated  $D_{2A}^1$  resonator with cross-section dimensions 22.86 mm by 10.16 mm, and a  $R$  of 159 mm, showing the charge on the surface of the resonator and the electric field pattern in the bulk of the resonator. (d) The normalised tangential azimuthal surface current density,  $|\mathbf{K}_{\beta\perp}|$ , of the resonant  $\text{TE}_{1,0,19.5}$  mode of the  $D_{2A}^1$  resonator and of (e) the resonant  $\text{TE}_{1,0,20}$  mode of the  $D_{2S}^1$  resonator. The antinode  $2n$  count is shown for both cases.

have half-integer  $n$ , confirming that the wavevector has returned  $\pi$  out of phase after completing one full circulation of the resonator. The surface plot of the  $\text{TE}_{1,0,20}$  mode in the  $D_{2S}^1$  resonator is shown in Fig. S12(e). The number of anti-nodes over one winding of the closed loop was  $N = 40$ , giving the integer azimuthal mode number  $n = N/2 = 20$ . This confirms as expected that the wavevector in the  $D_{2S}^1$  resonator has returned in phase; generating no  $\Pi_n$ .

The  $\text{TE}_{1,0,n}$  mode frequencies in both the  $D_{2A}^1$  and  $D_{2S}^1$  resonator follow the same modal spectrum. The frequencies of the half-integer modes in the  $D_{2A}^1$  resonator lie in the interim of the corresponding integer  $D_{2S}^1$  resonator modes. The accumulated  $\Pi_n$  is determined by the frequency shift required to align the half-integer modes with their integer counterparts. This leads to the following relationship:

$$\Pi_n = 2nR\pi(k_{n+\frac{1}{2}}^A - k_n^S), \quad (\text{S.61})$$

where  $k_{(n,j)+\frac{1}{2}}^A$  is the wavenumber of the  $\text{TE}_{1,0,(n,j)+\frac{1}{2}}$  mode in the  $D_{2A}^1$  resonator,  $k_{(n,j)}^S$  is the wavenumber of the  $\text{TE}_{1,0,n}$  mode in the  $D_{2S}^1$  resonator for integer  $n$ , and

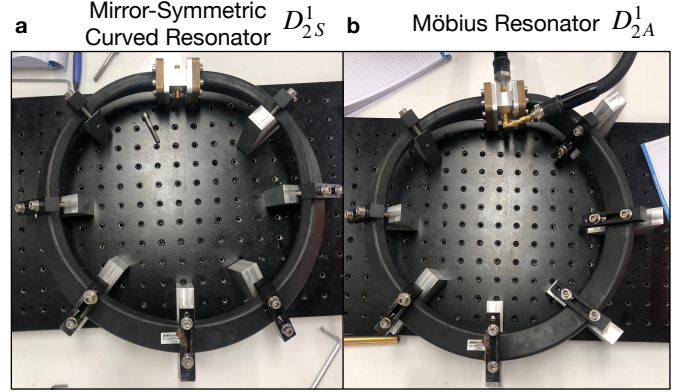


Figure S13. The experimental set-up of the (a)  $D_{2S}^1$  and the (b)  $D_{2A}^1$  cavities formed by bending a flexible waveguide around on itself and clamping it to angled edges to ensure the correct twist angle.

$R$  is the radius of both cavities.

Again, using the expression for group velocity  $V_g = \delta\omega/\delta k$ , we can express (S.61) in terms of the shift in resonant frequency,  $\Delta f_n$ , between the  $D_{2A}^1$  and  $D_{2S}^1$  resonator modes through the relationship:

$$\Pi_n = \Delta f_n \frac{4\pi^2 R}{V_g}, \quad (\text{S.62})$$

where  $\Delta f_n = f_{n+\frac{1}{2}}^A - f_n^S$ .

We can make this expression more explicit by using (S.24) and (S.25) and noting that for a  $D_2$  waveguide of side-length  $a$  and  $b$ , where  $a > b$ , the cutoff wavenumber is given by [46]

$$k_{cp} = \sqrt{\left(\frac{m\pi}{a}\right)^2 + \left(\frac{p\pi}{b}\right)^2}, \quad (\text{S.63})$$

which gives  $k_{cp}^R = \frac{\pi}{a}$  for the  $\text{TE}_{1,0,n}$  mode. The group velocity for the  $D_2$  twisted resonator can then be written as

$$V_g = c\sqrt{1 - \left(\frac{c}{2af_n^S}\right)^2}. \quad (\text{S.64})$$

Since the  $D_{2A}^{r\neq 0}$  resonator has the same transverse cross-sectional dimensions as the  $D_{2S}^r$  resonator they have the same  $V_g$ .

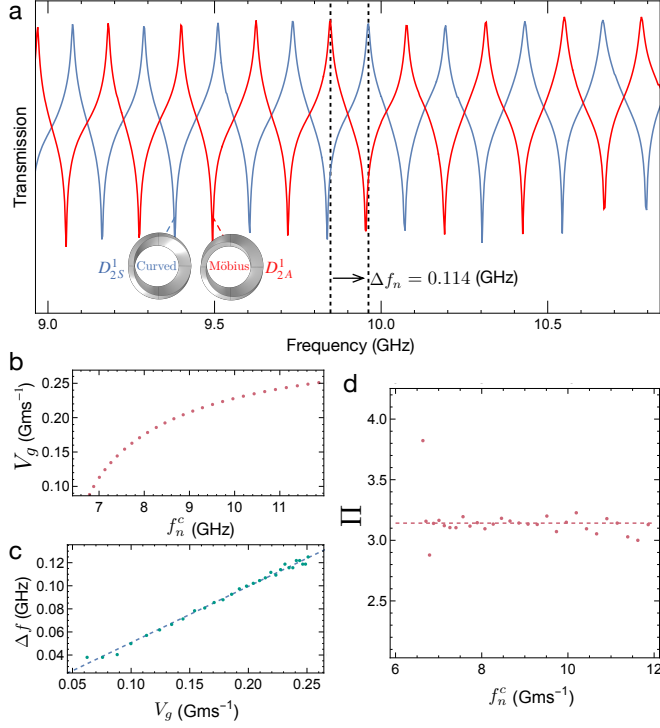


Figure S14. (a) The microwave transmission ( $S_{21}$ ) measured from the physically constructed  $D_{2S}^1$  resonator (blue) and the  $D_{2A}^1$  resonator (red). The frequency offset,  $\Delta f_n$ , between the two configurations is labelled by an arrow. (b) The  $D_{2S}^1$  resonant frequency  $f_n^S$  vs  $V_g$  showing that the wave speed increases with resonant frequency. (c) The linear relationship between  $\Delta f_n$  and  $V_g$ . (d) The measured  $\Pi_n$  vs  $f_n^S$ , which approaches a constant value of  $\pi$ .

We can now express the  $\Pi_n$  in a  $D_{2A}^1$  as:

$$\Pi_n = \Delta f_n \frac{4\pi^2 R}{c \sqrt{1 - \left(\frac{c}{2af_n^S}\right)^2}}. \quad (\text{S.65})$$

The resonant frequencies of the  $D_{2S}^1$  and  $D_{2A}^1$  resonators were measured, enabling an experimental observation of the spin-redirected Berry phase in the latter via relationship (S.65). This was achieved by constructing the physical cavity resonators and measuring their transmission. The  $D_{2S}^1$  resonator the waveguide was twisted  $\frac{\pi}{2}$  counter-clockwise (CCW) for one-half of the circumference, followed by a  $\frac{\pi}{2}$  clockwise (CW) twist for the other half, creating an absolute twist of  $\pi$  and a net twist of 0, as shown in Fig. S13(a). For the  $D_{2A}^1$  resonator configuration was constructed by twisting a flexible WR90 ( $a = 22.86$  mm by  $b = 10.16$  mm)  $D_2$  waveguide by  $\pi$  and connecting the ends of the waveguide with a straight portion of waveguide that seated two coaxial probes (see Fig. S13(b)). Both resonators had an approximate  $R$  of 159 mm.

As shown in Fig. S14(a), the transmission spectra of the  $D_{2A}^1$  resonator is offset from the  $D_{2S}^1$  resonator for the  $\text{TE}_{1,0,n}$  modes, giving direct evidence that a Berry phase is present. From Fig. S14(b), it can be seen that  $V_g$  increases with the resonant frequency and reaches a constant value at higher resonant frequencies. The relationship between  $V_g$  and  $\Delta f_n$  is linear (see Fig. S14(c)), as predicted by (S.62). Fig. S14(d) depicts how  $\Pi_n$  approaches a constant value of  $\pi$  for the  $\text{TE}_{1,0,n}$  modes in the microwave  $D_{2A}^1$  resonator, as predicted. This has previously only been observed in an optical Möbius cavity [3]. Since the polarisation over the photon path hasn't been varied this can be classified as a spin-redirected Berry phase.